Journal of Volcanology and Geothermal Research 440 (2023) 107852

Contents lists available at ScienceDirect

Journal of Volcanology and Geothermal Research

journal homepage: www.journals.elsevier.com/journal-of-volcanology-and-geothermal-research

Magnetotelluric investigations at Andean volcanoes: Partial melt or saline magmatic fluids?

A.P. Jenkins [a,*], A.C. Rust [a], J. Blundy [b], J. Biggs [a]

[a] School of Earth Sciences, University of Bristol, Wills Memorial Building, Queens Road, Bristol BS8 1RJ, United Kingdom
[b] Department of Earth Sciences, University of Oxford, South Parks Road, Oxford OX1 3AN, United Kingdom

ARTICLE INFO

Keywords:
Magnetotellurics
Volcano
Magmatism
Porphyry
Geothermal

ABSTRACT

Knowledge of the architecture of active magmatic systems is important for both volcanic hazard assessment and evaluating potential geothermal energy production and metals recovery from magmatic fluids. Increasingly, magmatic systems are imaged using the magnetotelluric method to detect electrically conductive partial melt and/or saline magmatic fluid reservoirs. We review recent magnetotelluric studies at eight Andean volcanoes, revealing electrical conductivity anomalies with variable magnitudes and locations. Six of the studied volcanoes exhibit three main electrical conductivity anomalies, located at shallow (<3 km), intermediate (≈5 km), and deep (>10 km) depths. The shallow anomalies are often thin and laterally extensive, consistent with clay cap alteration layers, while the deep anomalies are generally interpreted as partial melt reservoirs. The intermediate depth anomalies, although also often attributed to partial melt, have less clear origins. By analysing laboratory-derived electrical conductivity relationships, we show that the intermediate depth anomalies are generally most consistent with saline magmatic fluids stored in porous rock. However, other geophysical and petrological data suggest that localised partial melt also exists at intermediate depths. Therefore, the intermediate depth anomalies likely represent mixed melt and saline magmatic fluid systems, such as those responsible for forming magmatic-hydrothermal alteration zones and copper porphyry deposits. At individual volcanoes, refining the generalised three layer model proposed here by using additional geophysical or petrological data is key to constraining the resources and/or hazard potential of the magmatic system.

1. Introduction

In recent decades, perspectives on magma storage in Earth's crust have shifted away from shallow melt-dominated magma chambers towards the concept of low melt fraction systems that extend through the thickness of the crust (Cashman et al., 2017). Within this new framework, shallow melt-dominated reservoirs are believed to be transient features, with melt instead being heterogeneously distributed throughout a transcrustal magmatic system (Sparks and Cashman, 2017; Sparks et al., 2019; Edmonds et al., 2019). At active volcanoes, knowledge of the architecture of the magmatic system can therefore provide important context for volcano monitoring, with implications for anticipating eruption risk and associated volcanic hazards (Becerril et al., 2013; Chaussard and Amelung, 2014; Edmonds and Woods, 2018). Locating melt and exsolved saline magmatic fluid reservoirs is also of emerging industry interest, due to their potential as sources of high-enthalpy geothermal energy and a diverse portfolio of metals such as copper, gold, zinc, and rare earths (Reinsch et al., 2017; Watanabe et al., 2017; Blundy et al., 2021).

Direct identification of sub-surface melt or magmatic fluid is only possible by drilling into magmatic systems. Although geothermal energy projects exist near many volcanoes, drilling is mainly restricted to shallow hydrothermal systems driven by convecting meteoric or sea water, with little to no magmatic fluid input (Elders et al., 2014; Stimac et al., 2015; Kruszewski and Wittig, 2018). Few boreholes have penetrated into deeper melt or saline magmatic fluid reservoirs, which are typically isolated from overlying hydrothermal systems by a permeability barrier at the brittle-ductile transition, across which heat but little fluid is transferred (Fournier, 1999; Kasai et al., 1998; Elders et al., 2014; Blundy et al., 2021). The structure and nature of active magmatic systems are therefore poorly known, and studies must rely primarily on indirect methods such as petrological analyses of erupted material (Kesler et al., 2013; Cooper, 2019) and geophysical methods including seismic tomography, gravity surveying, and electromagnetic imaging

* Corresponding author.
E-mail address: alexander.jenkins@bristol.ac.uk (A.P. Jenkins).

https://doi.org/10.1016/j.jvolgeores.2023.107852
Received 16 January 2023; Received in revised form 23 June 2023; Accepted 27 June 2023
Available online 4 July 2023

(Magee et al., 2018). Understanding and integrating the information provided by each of these methods is key for furthering our understanding of magmatic systems. In particular, determining the identity of intergranular fluid phases using geophysical methods remains challenging, as silicate melts and saline fluids exhibit relatively similar physical properties.

In this study, we explore what the magnetotelluric method can reveal about melt and saline magmatic fluid reservoirs beneath volcanoes. We begin by reviewing the findings of recent magnetotelluric surveys at eight Andean volcanoes and summarising the features of the imaged electrical conductivity anomalies. To constrain the origins of these anomalies, we then review laboratory-derived electrical conductivity relationships for silicate melts and saline fluids, and we investigate the degree to which magnetotelluric studies can distinguish between partial melt and saline magmatic fluid reservoirs. To integrate the laboratory-derived relationships with the anomalies observed at Andean volcanoes, we then develop simplified models of magmatic systems and calculate their electrical conductivity structures as a function of the subsurface pressure and temperature conditions. Finally, we propose a generalised magmatic system model to explain the electrical conductivity anomalies observed at Andean volcanoes, and we discuss the implications for hazard assessment and resources potential.

2. Magnetotelluric investigations at volcanoes

2.1. The magnetotelluric method

Natural variations in Earth's magnetic field induce electric currents within the crust and mantle, with a magnitude that depends on the electrical resistivity. Magnetotelluric surveying involves measuring the time variations in the electric and magnetic fields at the Earth's surface, then using these data to determine the underlying electrical resistivity structure (Simpson and Bahr, 2005; Chave and Jones, 2012). For modern magnetotelluric surveys, researchers use computerised inversion to generate their preferred electrical resistivity model, which minimises both the misfit to the observed data and the model roughness. Magnetotelluric studies can investigate depths ranging from hundreds of meters to hundreds of kilometers, due to the wide frequency range over which the magnetic field varies; high frequency variations generated by lightening strikes sample the shallow structure, whereas low frequency variations caused by the interaction of the solar wind with the magnetosphere sample the deeper structure.

Magnetotelluric studies are particularly well suited to imaging magmatic systems because they are sensitive to the low electrical resistivity (i.e. high electrical conductivity) of both silicate melts and saline magmatic fluids relative to crustal rocks (Pommier and Le-Trong, 2011). Furthermore, depending on the spatial connectivity of melt or magmatic fluid within the host rock, only a small fluid fraction may be needed to generate a detectable electrical conductivity anomaly (i.e. a region of low electrical resistivity) (Glover et al., 2000). Magnetotelluric studies may therefore be able to detect the low melt fractions now thought to characterise many magmatic systems (Bachmann and Huber, 2016; Cooper, 2017). Consequently, the number of magnetotelluric studies being conducted at volcanoes has recently been increasing, making our review timely.

Despite their undoubted potential, magnetotelluric studies also have some important limitations. Most importantly, the inversion and interpretation of magnetotelluric data are non-unique, so different studies and methods may produce contrasting results. Common inversion methods also tend to smooth electrically conductive layers vertically, resulting in an imaged layer with greater vertical extent and lower electrical conductivity than the real layer (Cordell et al., 2022). Additionally, inversions are primarily sensitive to the electrical conductance of a layer rather than the electrical conductivity of the material in that layer, so electrically conductive layers will not be imaged if their electrical conductance is less than that of an overlying layer. Sensitivity analyses also show that magmatic bodies typically require dimensions of several kilometers to be detectable, depending on their electrical conductivity (Díaz et al., 2015; Piña-Varas et al., 2018; Cordell et al., 2018).

2.2. Magnetotelluric studies at Andean volcanoes

Magnetotelluric studies at volcanoes are typically conducted with a focus on either shallow hydrothermal systems from a geothermal energy perspective, or on the deeper magmatic system from a volcanic hazards or magmatic processes perspective. We restrict our review to the latter type, which includes studies using broadband and/or long-period magnetotelluric stations distributed across a large survey area, producing electrical resistivity models to a depth of $\geq$10 km. For consistency, we only consider studies that utilise 3D magnetotelluric methods. The Andean volcanic arc is the site of numerous recent studies meeting these criteria and thus represents an excellent case study for our review.

Using a literature search, we identify eight suitable magnetotelluric studies of Andean volcanoes, all of which are located within the Central and Southern volcanic zones. From north to south, they are: Paniri (Mancini et al., 2019), Uturuncu (Comeau et al., 2016), Láscar (Díaz et al., 2012), Lastarria (Díaz et al., 2015), Tinguiririca (Pearce et al., 2020), Laguna del Maule (Cordell et al., 2018), Villarrica (Pavez et al., 2020), and Osorno (Díaz et al., 2020). All of these studies display good spatial coverage of the volcano, except for Villarrica where only the northern flank was instrumented. The Paniri study area also covers the San Pedro-San Pablo and Cerro del Léon volcanoes, while the Tinguiririca study area includes the Planchón-Peteroa volcano. For studies covering multiple volcanoes, we select the volcano nearest to the imaged electrical conductivity anomalies as the representative volcano, although the anomalies themselves may be related to multiple overlapping volcanic systems.

Figure 1 shows a simplified summary of the electrical resistivity structures beneath the eight studied volcanoes, summarising the depths (below surface), magnitudes, and approximate spatial relations of the main imaged electrical conductivity anomalies, as well as any interpretations proposed in the original studies. Where possible, the electrical conductivity and depth values are taken directly from the original publication text. Otherwise, these values are estimated from the available figures (see Supplementary Material for a compilation of the original published images showing the electrical resistivity structure at each volcano). For each anomaly, we show only the maximum electrical conductivity, although in reality each anomaly is characterised by a range of electrical conductivities. Fig. 1 highlights the wide range of magnitudes, depths, and locations of the imaged electrical conductivity anomalies. However, it is also important to recognise the varied morphologies, erupted products, and levels of recent activity at the studied volcanoes, which could explain some of this variation. Differences between the resistivity models could also arise from the variable magnetotelluric datasets and inversion methods used at each volcano. For this reason, we consider only the main anomalies whose presence is confirmed by sensitivity testing in the original publications, as they are likely independent of the exact datasets and approaches used during inversion.

A prevalent feature in the magnetotelluric studies at Andean volcanoes is a relatively thin but often laterally extensive electrical conductivity anomaly located at shallow depths ($<$3 km), which is present beneath all of the volcanoes except Tinguiririca and Villarrica. These shallow anomalies generally have electrical conductivities of 0.1 to 1 S m^{-1}, although Uturuncu has a stronger shallow anomaly (1 to 10 S m^{-1}) and Osorno displays a weaker shallow anomaly (0.01 S m^{-1}). Due to their large lateral but limited vertical extent, the original studies generally attribute these shallow anomalies to clay minerals produced

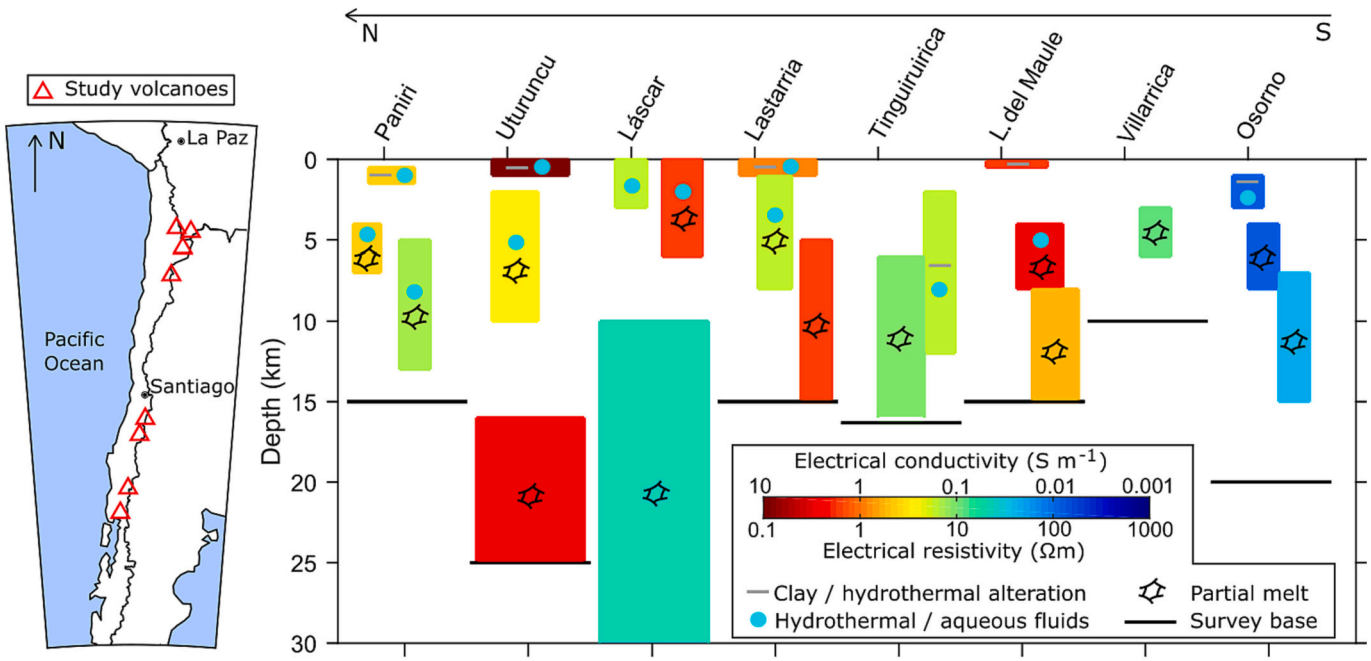

Reference	Mancini et al., 2019	Comeau et al., 2016	Díaz et al., 2012	Díaz et al., 2015	Pearce et al., 2020	Cordell et al., 2018	Pavez et al., 2020	Díaz et al., 2020
Other volcanoes in study	(San Pedro-San Pablo, Cerro del León)				(Planchón-Peteroa)			
Volcano morphology	Stratovolc (Stratovolc, domes)	Stratovolc	Stratovolc Domes	Stratovolc Domes	Stratovolc (Stratovolc, caldera)	Caldera Stratovolc Domes	Stratovolc Caldera	Stratovolc Domes Caldera
Last erupted	Pleistocene (1960?)	Pleistocene	2017	Holocene?	1917 (2019)	50 BC	2022	1869
Erupted products	And - Dac (BaA - Dac)	And - Dac	And - Dac	And - Dac	Bas - And (Bas - Dac)	Bas - Rhy	Bas - BaA	Bas - Dac
Number of MT stations	26 BB, 19 LP	96 BB	12 BB, 18 LP	30 BB, 11 LP	23 BB	71 BB	31 BB	16 BB
Period range in inversion (s)	0.00098-512, 100-3162	0.0087-1205	0.004-1000, 10-10000	0.02-370 30-3000	0.02-80 (?)	0.001-2000	0.0026-512	0.00098-1024
3D inversion code	ModEM	WSINV3DMT	WSINV3DMT	WSINV3DMT	ModEM	AA	ModEM	ModEM

Bas = basalt; BaA = basaltic-andesite; And = andesite; Dac = dacite; Rhy = rhyolite.
BB = broadband MT instrument; LP = long period MT instrument.
ModEM - Kelbert et al. (2014); WSINV3DMT - Siripunvaraporn et al. (2005); AA - Avdeev & Avdeeva (2009).

Fig. 1. Simplified representation of the electrical resistivity structures at the eight studied Andean volcanoes (see Supplementary Material for original published images). Depths are all kilometers below surface level. The anomalies are shaded according to their maximum electrical conductivity, with their approximate spatial relationships also illustrated (the tick marks show the edifice locations relative to the anomalies). The symbols show the interpretation for each anomaly given in the original publication. For studies covering multiple volcanoes, the characteristics of the other volcanoes are given in parentheses in the table.

by hydrothermal alteration, as electrically conductive smectite minerals break down at temperatures above around 200 °C (Beaufort et al., 2015; Stimac et al., 2015). However, hydrothermal fluids are also proposed to contribute to most of the shallow anomalies, perhaps reflecting the prevalence of hot springs and fumaroles. At Láscar, the shallow anomaly is interpreted exclusively as hydrothermal fluids. Tinguiririca does not display a typical shallow anomaly, although a hydrothermal system is instead interpreted from an anomaly located between 2 and 12 km depth, attributed to either fluids or clay minerals depending on whether the hydrothermal system is active or extinct.

At depths greater than a few kilometers, the electrical resistivity structures beneath Andean volcanoes are highly variable, although many deeper anomalies also have maximum electrical conductivities of 0.1 to 1 S m^{-1}. Interestingly, the strongest anomalies (>1 S m^{-1}) are located beneath Uturuncu and Laguna del Maule, which are among the least historically active and most silicic of the studied volcanoes. Weaker anomalies (<0.1 S m^{-1}) are located beneath Villarrica and Osorno, which display more mafic compositions.

All of the studied volcanoes except Villarrica display two electrical conductivity anomalies at depths greater than a few kilometers below the surface (Fig. 1). The first of these anomalies is located at intermediate depths (≈5 km) but can extend upwards to the surface (e.g. Láscar) and downwards to depths >10 km (e.g. Tinguiririca). The second of these anomalies is located deeper (>10 km), with its top generally at around 5–8 km depth. At Láscar and Uturuncu, the second anomaly is much deeper, beginning at 10 and 16 km depth respectively. The base of the deep anomaly is rarely imaged, only being resolved at Paniri and Osorno. At Villarrica, the absence of a deep anomaly could reflect the poor station coverage around the volcano, the shallow resolution limit of the survey, or the tendency of shallow electrically conductive structures to obscure deeper structures.

The geometry of the intermediate depth (≈5 km) anomalies varies from spherical or sill-like at Paniri, Láscar, Villarrica, and Osorno, through dipping structures at Lastarria, Laguna del Maule, and Tin-

guiruirica, to vertical at Uturuncu. By contrast, the deep (>10 km) anomalies are more voluminous, with both the lateral and vertical dimensions reaching 10s of km at Láscar and Uturuncu. Both the intermediate depth and deep anomalies are often laterally offset from the volcanic edifice; only Uturuncu and Osorno have intermediate depth anomalies directly beneath the volcano, while Láscar and Tinguiruirica have intermediate depth anomalies that extend >10 km from the edifice. Determining whether the intermediate depth and deep anomalies are connected is complicated due to the smoothing during inversion. However, a connection is imaged at Laguna del Maule, Tinguiruirica, and Osorno, while at Uturuncu the two anomalies are partly joined through a region of slightly lower electrical conductivity.

All of the original studies attribute the intermediate depth anomalies to the presence of partial melt, except for the intermediate depth anomaly at Tinguiruirica which is interpreted as a hydrothermal system. However, the studies at Paniri, Uturuncu and Laguna del Maule note that the intermediate depth anomalies have electrical conductivities that are difficult to explain with partial melt alone. Therefore, the additional presence of exsolved saline magmatic fluids, which are more electrically conductive than partial melt, is also suggested at intermediate depths at these volcanoes. The intermediate depth anomalies at Láscar and Lastarria are also interpreted as being caused by melt and/or magmatic fluids. By contrast, the original studies generally interpret the deep anomalies exclusively as partial melt, although the presence of additional fluids is suggested at Paniri.

2.3. Complementary petrological and geophysical data

To constrain the interpretation of magnetotelluric studies at Andean volcanoes, such as whether the intermediate depth (≈5 km) electrical conductivity anomalies represent partial melt or saline magmatic fluids, complementary data are required. For example, crystallisation depths calculated using geobarometry on volcanic products can be compared with the depths of the electrical conductivity anomalies. In the Andean magnetotelluric studies, concordant geobarometry depths are cited as evidence for partial melt generating the intermediate depth anomalies at Paniri (Cerro del León), Uturuncu, Laguna del Maule, and Villarrica (De Silva et al., 1994; Muir et al., 2014; Klug et al., 2020; Morgado et al., 2015), and the deep anomalies at Paniri, Uturuncu, and Laguna del Maule (Godoy et al., 2018; Sparks et al., 2008; Klug et al., 2020). However, geobarometry does not constrain the lateral dimensions of melt reservoirs and also pertains to the magmatic system at the time of crystallisation of the sample, which may not correspond with the present-day magmatic system.

By contrast, complementary geophysical methods provide present-day sub-surface images but suffer from the same ambiguity as magnetotelluric studies. For example, the deep electrical conductivity anomalies beneath Uturuncu and Láscar coincide with a large region of reduced seismic shear wave velocities ($-\Delta V_s > 30\%$) interpreted as the partially molten Altiplano-Puna magma body (Chmielowski et al., 1999; Zandt et al., 2003; Ward et al., 2014). Similarly, slow compressional wave velocities ($-\Delta V_p \approx 9\%$) beneath Villarrica overlap with the intermediate depth electrical conductivity anomaly and are also inferred to be of magmatic origin (Mora-Stock, 2015). By contrast, slow wave velocities that coincide with the intermediate depth electrical conductivity anomalies at Uturuncu ($-\Delta V_s \approx 10\%$) and Tinguiruirica ($-\Delta V_p >$ 6%) are attributed to hydrothermal systems instead (Jay et al., 2012; Pavez et al., 2016). At Lastarria, slow shear wave velocities ($-\Delta V_s =$ 23–63%) match remarkably well with all three electrical conductivity anomalies, and are interpreted as a shallow hydrothermal system overlying two deeper melt reservoirs (Spica et al., 2015).

Combining multiple geophysical datasets can help reduce uncertainties when interpreting active magmatic systems. For example, compelling evidence for a shallow (4 km) melt reservoir at Laguna del Maule is provided by overlapping slow shear and compressional wave velocities from seismic tomography ($-\Delta V_s =$ 12–28%, $-\Delta V_p =$ 9%), low densities from gravity surveys ($-\Delta\rho = 600$ kg m^{-3}), and a sill-like inflation source detected using InSAR (>25 cm / year uplift) (Bai et al., 2020; Wespestad et al., 2019; Miller et al., 2017; Feigl et al., 2014). However, no robust electrical conductivity anomaly is associated with this inferred melt reservoir (Cordell et al., 2018, 2020). Instead, a strong electrical conductivity anomaly (>1 S m^{-1}) is located 5 km to the north, rooted at greater depths but converging upwards towards the inferred melt reservoir. The high electrical conductivity of this anomaly, combined with the lack of associated gravity and seismic velocity anomalies, is consistent with saline magmatic fluids (Wespestad et al., 2019). In contrast, the inferred melt reservoir could go undetected by magnetotelluric studies if it has low temperature or water content (factors that reduce the electrical conductivity of silicate melts), especially as it is located beneath a highly electrically conductive clay cap (Cordell et al., 2020).

3. Origins of electrical conductivity anomalies

3.1. Effective electrical conductivity

Electrical conductivity anomalies beneath volcanoes are generally attributed to silicate melts, saline magmatic fluids, or electrically conductive minerals such as sulphides or some clays. In magmatic environments, clay and sulphide minerals form by alteration or precipitation from magmatic-hydrothermal fluids (Sillitoe, 2010), which in turn are derived from volatiles exsolved from silicate melts (Audétat and Edmonds, 2020; Tattitch et al., 2021). Because of this genetic link, the phases responsible for generating electrical conductivity anomalies beneath volcanoes may be somewhat spatially coincident, although a general transition from deeper melt reservoirs, through overlying exsolved saline magmatic fluids, to shallower mineralisation and alteration may be expected. With magnetotelluric data alone, it is generally impossible to uniquely determine the cause of an electrical conductivity anomaly. However, the origins of electrical conductivity anomalies can be better constrained by using knowledge of the electrical conductivities displayed by common electrically conductive phases.

The electrical conductivity of common electrically conductive phases can be measured in the laboratory as a function of temperature, pressure, and composition (Laštovičková, 1991; Ni et al., 2014). However, electrically conductive phases generally constitute only a proportion of a given rock mass, so the relevant parameter for magnetotelluric data interpretation is the effective electrical conductivity of the rock mass as a whole. The effective electrical conductivity depends on both the proportion and spatial connectivity of the electrically conductive phase(s) within the host rock. Different levels of spatial connectivity are represented by different geometrical mixing models or can be characterised by empirical relationships (Table 1) (Glover et al., 2000). Depending on which mixing model is used, the calculated effective electrical conductivity can vary greatly. For simplicity, and due to the lack of laboratory data for multiphase mixing, we only consider two-phase systems here (i.e. host rock + one conductive phase).

To constrain the origins of the intermediate depth (≈5 km) and deep (>10 km) electrical conductivity anomalies at Andean volcanoes, we review the laboratory-determined electrical conductivities of saline fluids and silicate melts and discuss the appropriate mixing models. Although drilling results show that smectite-rich layers within argillic alteration zones generate the laterally extensive shallow electrical conductivity anomalies beneath volcanoes (Ryan et al., 2013; Bertrand et al., 2012; Lee et al., 2020), smectite is only stable at temperatures <180–240 °C (Stimac et al., 2015), so it is unlikely to contribute to the intermediate depth and deep anomalies. In theory, sulphide minerals could contribute to these anomalies; however, the available data suggests that sulphides do not exhibit sufficiently high spatial connectivity to generate the observed electrical conductivity anomalies (Supplementary Material). A high content of sulphide minerals would also

Table 1
Mixing models for effective electrical conductivity (σ_{Eff}) in two-phase media, in order of decreasing spatial connectivity and effective electrical conductivity (electrical conductivity is the inverse of electrical resistivity).

Name	σ_{Eff} =	Visualisation	Reference
Parallel model	$(1-X_2)\sigma_1 + X_2\sigma_2$	Layers arranged parallel to electric current direction.	Guéguen and Palciauskas (1994)
Hashin-Shtrikman (HS) upper bound	$\sigma_2\left(1-\frac{3(1-X_2)(\sigma_2-\sigma_1)}{3\sigma_2-X_2(\sigma_2-\sigma_1)}\right)$	Space-filling spheres with a core of host rock and rim of electrically conductive phase.	Hashin and Shtrikman (1962)
Films model	$(1-X_2)\sigma_1 + \frac{2}{3}X_2\sigma_2$	Completely wetted films of electrically conductive phase along host rock grain boundaries.	Waff (1974)
Tubes model	$(1-X_2)\sigma_1 + \frac{1}{3}X_2\sigma_2$	Tubes of electrically conductive phase along host rock triple junctions.	Grant and West (1965)
Hashin-Shtrikman (HS) lower bound	$\sigma_1\left(1+\frac{3X_2(\sigma_2-\sigma_1)}{3\sigma_1+(1-X_2)(\sigma_2-\sigma_1)}\right)$	Space-filling spheres with a core of electrically conductive phase and rim of host rock.	Hashin and Shtrikman (1962)
Perpendicular model	$\left(\frac{1-X_2}{\sigma_1}+\frac{X_2}{\sigma_2}\right)^{-1}$	Layers arranged normal to electric current direction.	Guéguen and Palciauskas (1994)
Modified Archie's Law	$(1-X_2)^p\sigma_1 + X_2^m\sigma_2$ $p=\frac{log_{10}(1-X_2^m)}{log_{10}(1-X_2)}$	Empirical relationship with conductive phase connectivity defined by m.	Glover et al. (2000)

σ_{eff} = Effective electrical conductivity; σ_1 = Host rock electrical conductivity; σ_2 = Conductive phase electrical conductivity; X_2 = Proportion of electrically conductive phase. (Archie's Law is an empirically determined relationship, not a geometrical mixing model.)

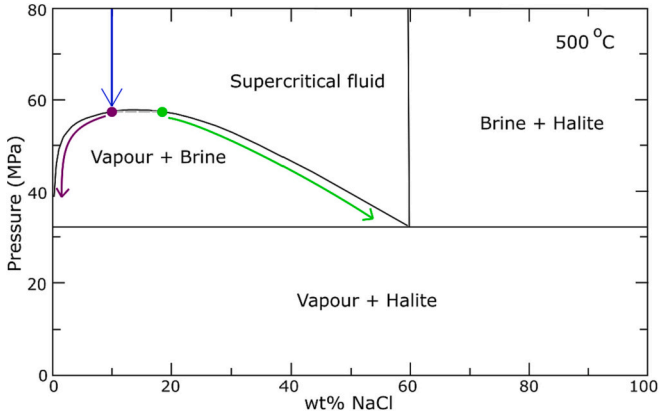

Fig. 2. Phase changes for ascending supercritical saline magmatic fluids with a bulk salinity of 10 wt% NaCl (blue), assuming a constant fluid temperature of 500 °C. When pressure decreases to 57 MPa, the supercritical fluid separates into coexisting vapour (purple) and hypersaline brine (green) phases, with salinities of 10 and 18 wt% NaCl respectively. Continued pressure decrease drives the vapour phase to progressively lower salinity and the brine phase to progressively higher salinity. At 32 MPa, a further phase transition occurs due to halite precipitation. Phase boundaries from Driesner and Heinrich (2007). (For interpretation of the references to colour in this figure legend, the reader is referred to the web version of this article.)

produce an elevated density that would likely be detectable by gravity surveys. Graphite may also confer high electrical conductivity to rocks, especially when distributed as thin films (Glover, 1996). However, this situation is most relevant to metamorphic rocks; crustal igneous rocks are rarely sufficiently reduced for graphite to be stable.

3.2. Saline magmatic fluids

Saline magmatic fluids conduct electricity through the movement of dissolved ions, so ionic strength (or salinity) is the strongest control on their electrical conductivity. Fluids exsolved directly from melt reservoirs are typically in a supercritical state with salinities in the range of 5–15 wt% $NaCl_{eq}$ (Heinrich, 2005; Audétat and Edmonds, 2020; Tattitch et al., 2021). However, as these fluids ascend to shallower depths, pressure decrease can trigger phase separation into coexisting hypersaline brine ($\gtrsim$20 wt% $NaCl_{eq}$) and low salinity vapour phases (Fig. 2) (Driesner and Heinrich, 2007). The pressure (depth) at which phase separation occurs depends on temperature. The dense brine, which is more likely to be retained in pore space within the host rock, can be many times more saline than the initial magmatic fluid. Further pressure decrease can lead to the formation of coexisting vapour and halite phases.

Taking the NaCl content of a solution as a proxy for total salinity, the electrical conductivity of saline magmatic fluids under crustal pressure and temperature conditions can be calculated using the empirical relationship of Watanabe et al. (2021) (Table 2). Although no electrical conductivity measurements have been conducted on hypersaline brines, the relationship of Watanabe et al. (2021) can be extrapolated to estimate their electrical conductivity. By contrast, the relationship of

Table 2
NaCl solution empirical electrical conductivity relationships under crustal conditions.

Model	Fluid	Salinity (wt %)	Temperature (°C)	Pressure (GPa)
Sinmyo and Keppler (2017)	NaCl	0.058–5.63	100–600	0.0001–1
Watanabe et al. (2021)	NaCl	0.06–24.6	20–525	0.0025–0.2

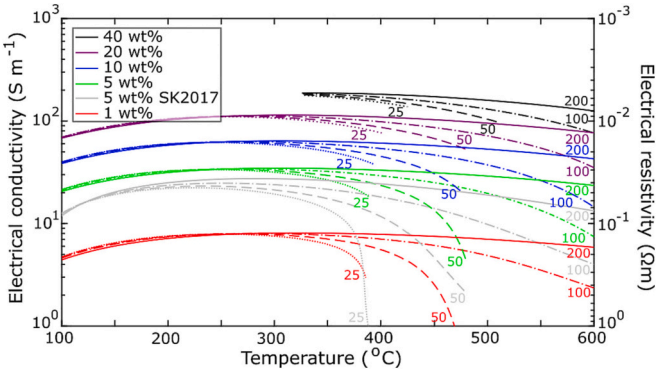

Fig. 3. Electrical conductivity of NaCl solution as a function of temperature, calculated using the relationship of Watanabe et al. (2021). Colour indicates salinity, while the numbers and line styles show pressure in MPa. The plots are calculated only where a liquid or supercritical fluid phase exists with the specified salinity. The electrical conductivity of 5 wt% NaCl solution calculated using Sinmyo and Keppler (2017) is also shown in grey.

Sinmyo and Keppler (2017) does not produce reasonable electrical conductivities if phase separation occurs, and Watanabe et al. (2021) state that extrapolation of the Sinmyo and Keppler (2017) model to salinities >5 wt% NaCl causes an underestimation of the electrical conductivity.

Figure 3 shows how the electrical conductivity of NaCl solution increases with increasing salinity, due to higher concentrations of charge-carrying ions. Typical supercritical fluids (5–15 wt% $NaCl_{eq}$) exsolved from magmas have electrical conductivities on the order of 10^1 S m^{-1}, whereas hypersaline brines (≳20 wt% $NaCl_{eq}$) formed by phase separation of this fluid are predicted to have electrical conductivities on the order of 10^2 S m^{-1}. Temperature and pressure have complex effects on the electrical conductivity of NaCl solution. For any given salinity, the electrical conductivity reaches a maximum at around 250–300 °C, independent of pressure, due to an increase in charge-carrier mobility with temperature (Quist and Marshall, 1968; Sinmyo and Keppler, 2017; Watanabe et al., 2021). Above approximately 300 °C, pressure also becomes an important control. At lower pressures, the electrical conductivity decreases with increasing temperature, due to a combination of fluid expansion decreasing the number of ions per unit volume and a decrease in the dielectric constant of water (Watanabe et al., 2021). At higher pressures, the peak electrical conductivity is maintained towards higher temperatures, as the increased pressure reduces fluid expansion while also increasing the dielectric constant of water (Sinmyo and Keppler, 2017; Watanabe et al., 2021).

The spatial connectivity of saline pore fluids likely varies with host rock lithology. However, studies on the electrical conductivity of fluid-bearing rocks focus on hydrocarbon reservoir rocks. Fig. 4a shows the electrical conductivity of clean sandstones saturated with 4 wt% NaCl solution, measured in the laboratory at ambient conditions (Gomez et al., 2010). Mixing models (Table 1) using the measured electrical conductivity of the saturating fluid (5.9 S m^{-1}) show that the fluid spatial connectivity is relatively high and increases with fluid fraction; at porosities below around 0.15, the electrical conductivity is around one tenth of the value given by the HS upper bound mixing model, whereas the tubes mixing model is appropriate at porosities above 0.15.

Similarly, Fig. 4b shows the electrical conductivity of sandstones with a variable clay content (0–28%) saturated with 3.5 wt% NaCl solution at 26 MPa and ambient temperature (Han et al., 2015). Despite the increased clay content and confining pressure, mixing models using the measured electrical conductivity of the saturating fluid (4.7 S m^{-1}) show similar spatial connectivity to that of clean sandstones (Fig. 4a), suggesting that saline fluid connectivity is relatively high under a variety of conditions. However, the data in Fig. 4 only consider clastic sedimentary rocks, and fluid connectivity in magmatic systems could

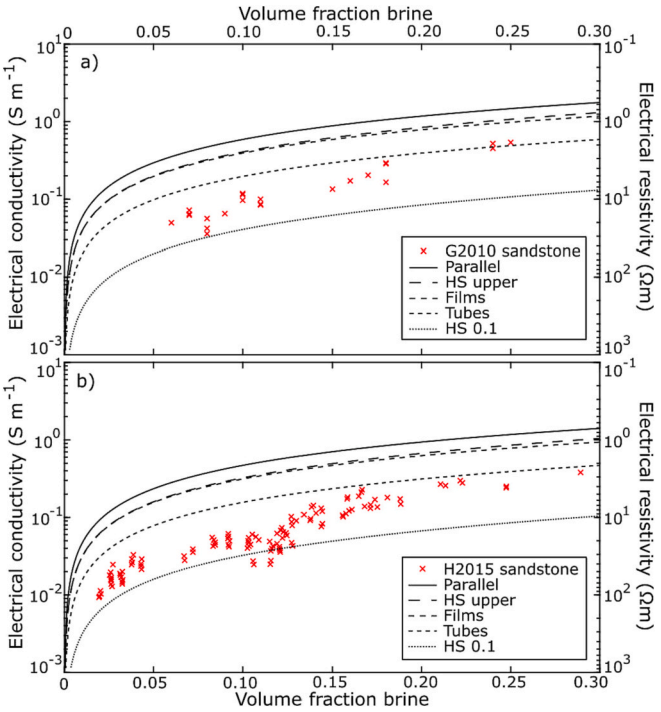

Fig. 4. Electrical conductivity of sandstones saturated with NaCl solution as a function of porosity. a) Clean sandstones saturated with 4 wt% NaCl solution at ambient conditions, with fully-saturated electrical conductivity calculated from partially-saturated electrical conductivity using Archie's equation (Gomez et al., 2010). b) Sandstones with variable clay content (0–28%) fully-saturated with 3.5 wt% NaCl solution at 26 MPa and ambient temperature (Han et al., 2015). The shown mixing models use the measured electrical conductivity of the saturating fluid (5.9 S m^{-1} in a; 4.7 S m^{-1} in b) and are insensitive to the negligible host rock electrical conductivity. HS 0.1 models an electrical conductivity equal to one tenth of the value given by the Hashin-Shtrikman upper bound mixing model.

differ and requires further study. Conceptually, the typically lower permeability of igneous rocks may mean that fluid spatial connectivity is lower. However, high fluid connectivity at low fluid fractions may be feasible if the fluid is wetting and forms films along grain boundaries.

3.3. Silicate melts

Silicate melts are also ionic electrical conductors, with Na^+ the dominant charge carrier except in some hydrous mafic and intermediate melts (Gaillard, 2004; Guo et al., 2016, 2017). The electrical conductivity of silicate melts is complex, being strongly dependent on temperature, composition, and water content, with pressure generally less important (Zhang et al., 2021). Carbon dioxide content may also effect melt electrical conductivity, but this is poorly constrained and likely less important than water content (Ni et al., 2011). Overall, melt electrical conductivity increases with increasing temperature and water content, but decreases with increasing pressure (Guo et al., 2017). At mantle conditions, melt electrical conductivity generally decreases with increasing silica content (Zhang et al., 2021). However, melt differentiation in the crust leads to silicic melts that are cooler but also more water-rich than their more mafic parental melts, complicating how silica content alone correlates with electrical conductivity.

Currently, the only generalised empirical melt electrical conductivity relationship is the SIGMELTS model of Pommier and Le-Trong (2011), which calculates melt electrical conductivity as a function of temperature, pressure, and SiO_2, Na_2O, and H_2O contents. However, more recent experiments have shown that SIGMELTS significantly overestimates electrical conductivity for melts with low water contents and

Table 3
Empirical silicate melt electrical conductivity relationships.

Model	Composition	SiO_2 (wt%)	Na_2O (wt%)	Temperature (°C)	Pressure (GPa)	H_2O (wt%)
Pommier and Le-Trong (2011)	General	49.2–55.7	2.0–6.1	400–1300	0–0.4	0–5.6
Ni et al. (2011)	Basaltic	50.1	3.7	1200–1650	2.0	0–6.0
Laumonier et al. (2017)	Andesitic	60.9	2.1	910–1407	0.5–3.0	0–9.0
Guo et al. (2017)	Andesitic	60.8	3.2	890–1300	0.5–1.0	0–5.9
Laumonier et al. (2015)	Dacitic	67.9	2.1	400–1350	0.3–3.0	0–11.8
Guo et al. (2016)	Rhyolitic	75.7	4.7	595–1392	0.5–1.0	0.1–7.9

SiO_2 and Na_2O are wt% anhydrous.

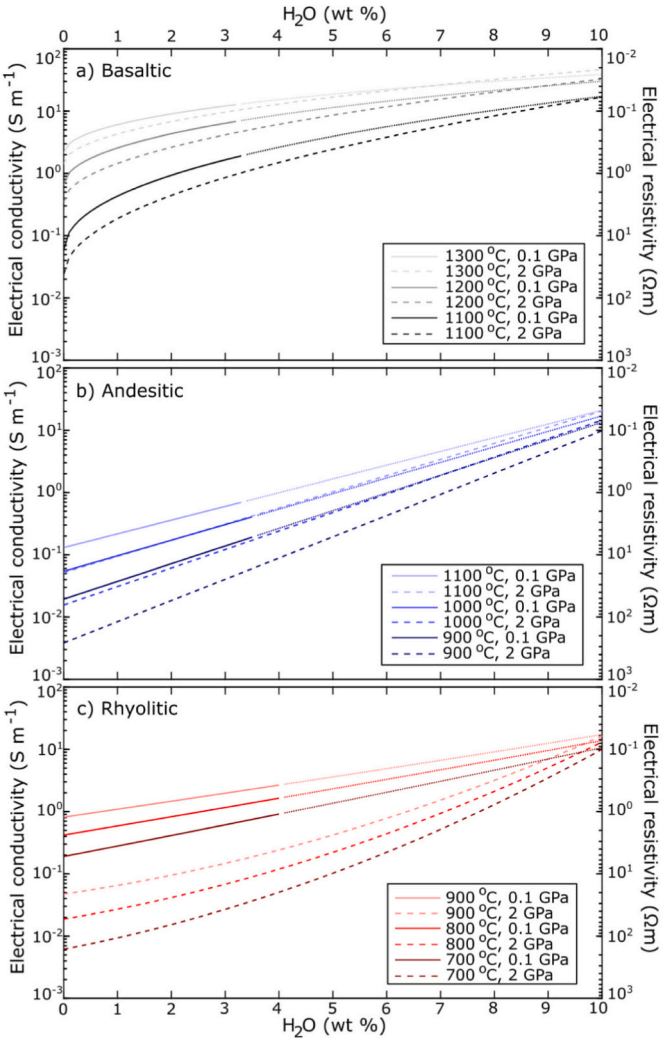

Fig. 5. Silicate melt electrical conductivity calculated from the fixed melt composition relationships as a function of water content at a range of representative temperatures and pressure of 0.1 and 2 GPa. Dotted lines represent where water saturation is exceeded for the 0.1 GPa case. a) Basaltic (Ni et al., 2011), b) Andesitic (Laumonier et al., 2017), c) Rhyolitic (Guo et al., 2016).

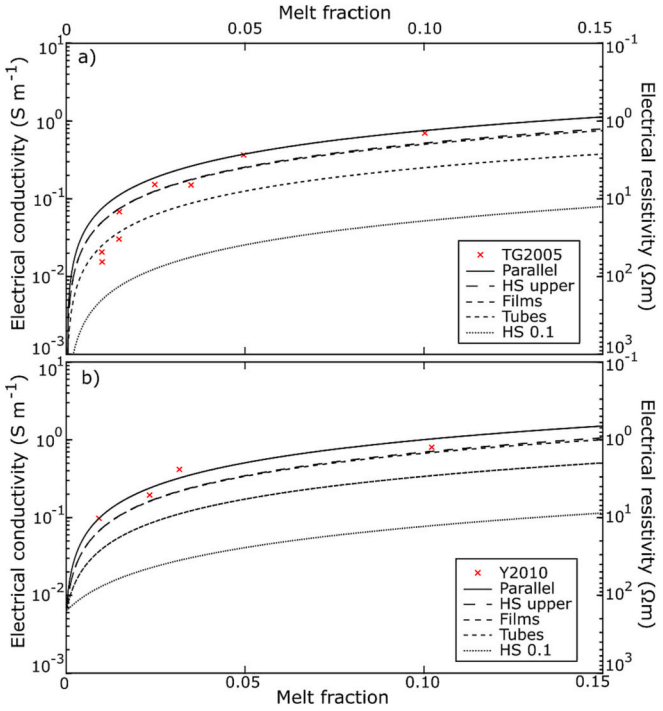

Fig. 6. Electrical conductivity of melt-bearing rocks as a function of melt fraction. a) Synthetic iron-free olivine rocks with synthetic basaltic melt at 1475 °C and atmospheric pressure (ten Grotenhuis et al., 2005). b) San Carlos olivine with mid-ocean ridge basaltic melt at 1326 °C and 1.5 GPa (Yoshino et al., 2010). The mixing models use the measured melt electrical conductivity of 7.5 S m^{-1} in a), and the defined melt electrical conductivity of 10 S m^{-1} in b). The shown mixing models are insensitive to the low host rock electrical conductivity. HS 0.1 models an electrical conductivity equal to one tenth of the value given by the Hashin-Shtrikman upper bound mixing model.

significantly underestimates electrical conductivity for melts with high water contents (Guo et al., 2017; Zhang et al., 2021). Users of SIGMELTS must also account for a number of discontinuities that arise during interpolation, which are clearly non-physical. Therefore, we prefer to use fixed melt composition empirical electrical conductivity relationships, which are available for a range of melt compositions as a function of temperature, pressure, and water content (Table 3). These relationships are calibrated at high pressures only (>500 MPa), so they must be extrapolated to shallow crustal pressures. Guo et al. (2016) state that extrapolation of their relationship for rhyolitic melts to lower pressures is likely valid, while pressure is less important for andesitic and basaltic melts (Zhang et al., 2021).

Figure 5 shows melt electrical conductivities calculated using the fixed composition relationships for basaltic, andesitic, and rhyolitic melts (Table 3) as a function of water content and at pressures of 2 GPa (≈70 km) and 0.1 GPa (≈4 km). We use representative temperatures of 700–900 °C for rhyolitic melts, 900–1100 °C for andesitic melts, and 1100–1300 °C for basaltic melts (Lesher and Spera, 2015). The relationship of Ni et al. (2011) for basaltic melts does not account for pressure, so we approximate basaltic melt electrical conductivity below 2 GPa by applying the same relative increase in electrical conductivity as for andesitic melts between 2 GPa and the specified pressure, using the relationship of Laumonier et al. (2017) at the specified temperature. The relationship of Laumonier et al. (2017) is preferred to that of Guo et al. (2017) for andesitic melts because it is calibrated to a higher water content (Table 3).

Figure 5 shows that basaltic melts generally display the highest electrical conductivities due to their higher temperatures. The importance of melt composition, in particular the sodium content, is shown by

the lower electrical conductivities of andesitic melts compared with basaltic and rhyolitic melts, as the relationship of Laumonier et al. (2017) for andesite is based on a relatively sodium-poor composition (Table 3). Water content also exerts a very strong control on melt electrical conductivities, which converge at very high water contents. Water content and temperature have a greater effect on electrical conductivity for basic melts compared to silicic melts. Conversely, pressure exerts a stronger control on electrical conductivity for rhyolitic melts compared to andesitic melts. Overall, most crustal melts likely have electrical conductivities on the order of 10^0 S m^{-1} or less, with only very hot or very water-rich melts having electrical conductivities on the order of 10^1 S m^{-1}.

In melt storage zones, melt spatial connectivity is a function of the interfacial energies at melt-grain boundaries (Daines and Pec, 2015). Fig. 6a shows the electrical conductivity of synthetic olivine rocks with added synthetic basaltic melt at 1475 °C and atmospheric pressure, measured in the laboratory (ten Grotenhuis et al., 2005). Mixing models (Table 1) using the measured melt electrical conductivity (7.5 S m^{-1}) show that melt spatial connectivity is very high and increases with melt fraction (e.g. Samrock et al., 2021). At low melt fractions (<0.02), the electrical conductivity is well modelled by the tubes mixing model, whereas at intermediate melt fractions the films or HS upper bound models are suitable, and at higher melt fractions (>0.05) the parallel model is appropriate.

Similarly, Fig. 6b shows the electrical conductivity of San Carlos olivine with added mid-ocean ridge basaltic melt at 1326 °C and 1.5 GPa (Yoshino et al., 2010). Despite the vastly increased pressure, mixing models using the defined melt electrical conductivity (10 S m^{-1}) show that the melt spatial connectivity is extremely high, with the electrical conductivity well modelled by the HS upper bound or parallel mixing models at all melt fractions studied. However, Fig. 6 shows olivine rocks only; melt connectivity in more silicic rocks may be lower and requires further investigation, as more melt is needed to form an interconnected network in silicic rocks than in mafic rocks (Vigneresse et al., 1996; Rosenberg and Handy, 2005).

4. Interpreting electrical conductivity anomalies

4.1. Silicate melt or saline magmatic fluids?

At depths greater than typical clay caps (>2–3 km), electrical conductivity anomalies of mostly 0.1 to 1 S m^{-1} beneath volcanoes are usually attributed to the presence of melt and/or fluids (Fig. 1). However, whether an anomaly is interpreted as silicate melt or as saline magmatic fluids has important implications. While some studies offer a preferred interpretation, often no such distinction is made (e.g. Díaz et al., 2012, 2015; Mancini et al., 2019). Although distinguishing between melt and magmatic fluids from magnetotelluric data alone is difficult, we have shown that saline magmatic fluids generally have higher electrical conductivities (10^1 S m^{-1} for primary magmatic fluids, 10^2 S m^{-1} for hypersaline brines) than typical crustal melts (10^{-2}-10^0 S m^{-1} for most melts, 10^1 S m^{-1} for very wet or very hot melts). Therefore, an important question is whether partial melt reservoirs can generate sufficiently high electrical conductivities, assuming appropriate mixing models and physical parameters, to explain the electrical conductivity anomalies observed beneath volcanoes. If partial melt cannot explain the observed anomalies, saline magmatic fluids are likely responsible instead. This is particularly relevant for intermediate depth (≈5 km) electrical conductivity anomalies, which could represent either potentially economically important saline fluids or potentially hazardous melt reservoirs.

To investigate this, we use the fixed melt composition electrical conductivity relationships to calculate the theoretical maximum electrical conductivities for anomalies generated by partial melt. The maximum electrical conductivity of silicate melts increases with depth, due to increasing water solubility in melts with increasing pressure.

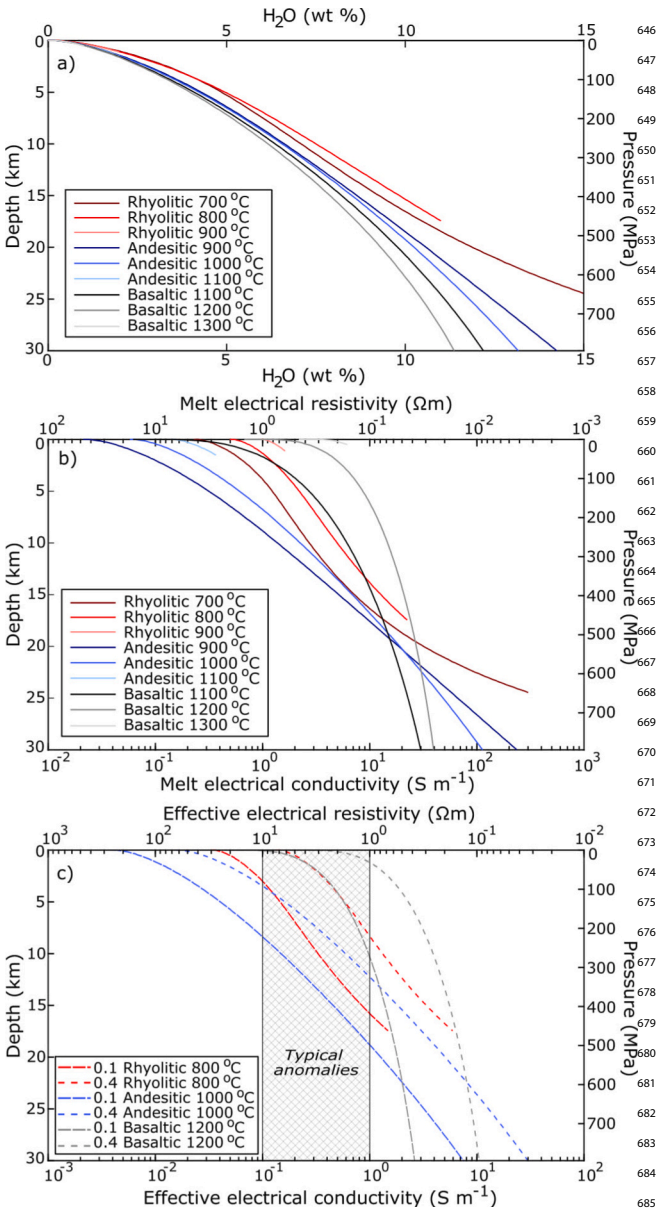

Fig. 7. a) Water solubility in melts as a function of depth, calculated using MagmaSat (Ghiorso and Gualda, 2015) and assuming a lithostatic pressure gradient with a high crustal density of 2700 kg m^{-3}. For water contents exceeding 1–2%, the highest representative melt temperatures (900 °C rhyolitic, 1100 °C andesitic, 1300 °C basaltic) exceed their respective melt liquidus temperatures; this also occurs for 800 °C rhyolitic melt at water contents >11%. b) Maximum melt electrical conductivity as a function of depth, calculated using the fixed composition melt electrical conductivity models (Ni et al., 2011; Laumonier et al., 2017; Guo et al., 2016) and assuming water-saturated melts (up to either 15 wt% H_2O or the water content at which the melt liquidus temperature falls below the melt temperature) under a lithostatic pressure gradient with a crustal density of 2700 kg m^{-3}. c) Maximum electrical conductivity of partial melt as a function of depth, assuming the films mixing model with melt fractions of 0.1 and 0.4 and a host rock with negligible electrical conductivity. For clarity, only the highest representative melt temperature for which the liquidus is not rapidly exceeded is shown for each melt composition. Note the different electrical conductivity scale from b) to c).

However, water solubility in melts also depends on the melt composition and temperature, which themselves affect the melt electrical conductivity. Furthermore, increasing the water content in melts also lowers the melt liquidus temperature, which under normal geological circumstances acts as an upper limit on the melt temperature. To account for

these interdependencies, we therefore consider a range of melt compositions and temperatures.

For consistency, we use the major oxide melt compositions from the electrical conductivity relationships for basaltic, andesitic, and rhyolitic melts (Ni et al., 2011; Laumonier et al., 2017; Guo et al., 2016) (Table 3) and the same representative temperatures as in Fig. 5. We first input these compositions and temperatures to the MagmaSat model (Ghiorso and Gualda, 2015) within VESIcal (Iacovino et al., 2021) to calculate saturation pressures for water contents up to either 15 wt% or the water content at which the melt liquidus temperature falls below the melt temperature (Gualda and Ghiorso, 2015). For each water content, we use the 'fixed volatiles' normalisation, which maintains the specified water content and scales the major oxide contents so that the system as a whole (including water) totals 100 wt%. To convert the saturation pressures to saturation depths, we define a lithostatic pressure gradient with a high crustal density of 2700 kg m^{-3}, thereby maximising water solubility as a function of depth (Fig. 7a).

For each melt composition and temperature, we then use the corresponding fixed melt composition electrical conductivity relationship to calculate the maximum electrical conductivity of the melt as a function of depth, by assuming water saturation in the melt (Fig. 7b). Electrical conductivity anomalies generated by 100% melt could match those shown in Fig. 7b. However, geophysical, geochemical, and geological observations suggest that crustal melts are generally stored as crystal-rich mushes (Bachmann and Huber, 2016; Magee et al., 2018). Therefore, we calculate the maximum electrical conductivities for partial melts by using the films mixing model, which we consider to give the highest reasonable melt spatial connectivity. We use a melt fraction of 0.1 to represent a typical mushy system, and a melt fraction of 0.4 to represent a very melt-rich mush (Fig. 7c) (Sparks et al., 2019).

Figure 7a shows that water solubility in melts decreases with increasing melt temperature. Despite this, the electrical conductivity of water-saturated melts generally increases with increasing melt temperature (Fig. 7b). However, for water contents >1–2%, the highest representative melt temperatures used (900 °C rhyolitic, 1100 °C andesitic, 1300 °C basaltic) exceed their respective liquidus temperatures and so are geologically unreasonable. Therefore, we report the maximum electrical conductivity anomalies that can be generated by melts using representative temperatures of 800 °C for rhyolite, 1000 °C for andesite, and 1200 °C for basalt.

Figure 7b shows that for depths <15 km, water-saturated basaltic melts have the highest electrical conductivities due to their higher temperatures, typically being on the order of 10^0 S m^{-1} at 1100 °C and 10^1 S m^{-1} at 1200 °C. By contrast, water-saturated andesitic and rhyolitic melts have lower electrical conductivities generally on the order of 10^{-1}-10^0 S m^{-1}. However, with increasing depth, the higher water solubility in andesitic and rhyolitic melts (Fig. 7a) causes their maximum electrical conductivities to exceed those of basaltic melts. At depths >15 km, the electrical conductivities of water-saturated andesitic and rhyolitic melts are on the order of 10^1 S m^{-1}, potentially reaching 10^2 S m^{-1} at even greater depths. Whether deep andesitic and rhyolitic melts can have electrical conductivities on the order of 10^2 S m^{-1} in reality is unclear, as this would require melts with water contents >12 wt%. Although some evidence exists for such superhydrous melts (e.g. Krawczynski et al., 2012; Goltz et al., 2020; Müntener et al., 2021), their widespread presence is unconfirmed. Additionally, the calculations for superhydrous melts exceed the calibrated water contents in both MagmaSat and the fixed composition electrical conductivity models.

Using the films mixing model, a mush with a high melt fraction of 0.4 has an electrical conductivity approximately half an order of magnitude lower (73%) than pure melt. Nonetheless, electrical conductivity anomalies of 0.1 S m^{-1} at any depth beneath volcanoes can be explained by basaltic or rhyolitic partial melts, although andesitic partial melt cannot explain anomalies of 0.1 S m^{-1} at depths <4 km (Fig. 7c). By contrast, anomalies of 1 S m^{-1} at depths <8 km can only be explained by basaltic partial melts. We consider that the electrical conductivity

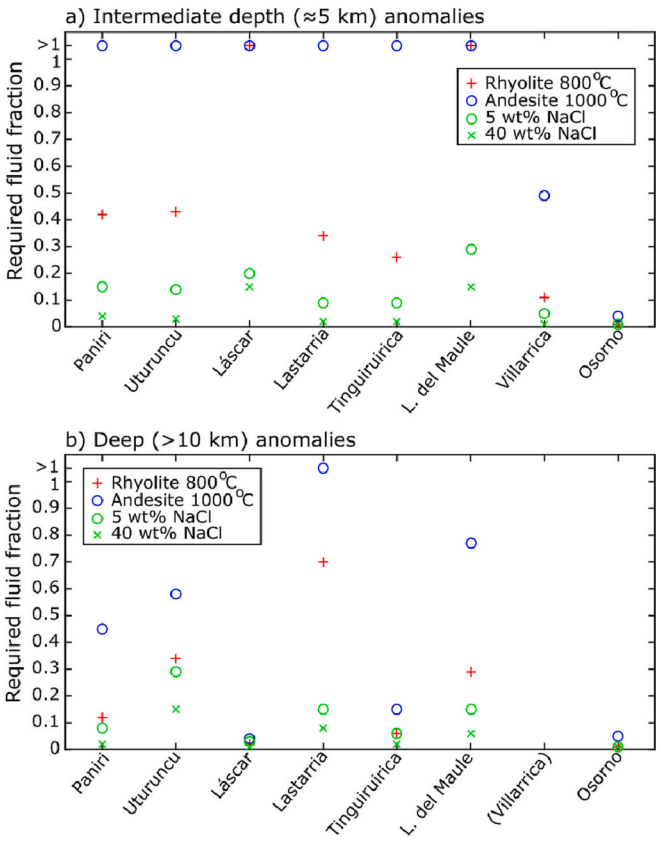

Fig. 8. Fluid fractions of representative silicate melts and saline magmatic fluids required to explain a) the intermediate depth (≈5 km), and b) the deep (>10 km) electrical conductivity anomalies at the studied Andean volcanoes. For melts, this assumes water saturation at the top of each anomaly and the films mixing model. For saline fluids, this assumes the peak electrical conductivity values from Fig. 3 and electrical conductivities equal to one tenth of the value given by the HS upper bound mixing model for fluid fractions <0.15 and the tubes mixing model for fluid fractions >0.15. All calculations use a lithostatic pressure gradient with a crustal density of 2700 kg m^{-3} and a host rock with negligible electrical conductivity. No deep anomaly is imaged at Villarrica. See Supplementary Material for more detail.

profiles in Fig. 7c represent the maximum reasonable values attributable to the presence of partial melt beneath most volcanoes. Only in exceptional circumstances, such as for highly sodic melts or melt fractions above 0.4, are these values likely to be exceeded. In reality, electrical conductivity anomalies caused by melt may be significantly lower. For example, a more conservative melt fraction of 0.1, such as that proposed for the Altiplano-Puna magma body from seismic tomography (Pritchard et al., 2018), reduces the electrical conductivity by over an order of magnitude (93%) relative to pure melt. A melt fraction of 0.1 cannot explain electrical conductivity anomalies of 1 S m^{-1} at depths <10 km for any melt composition (Fig. 7c).

To extend this method to investigate the origins of the intermediate depth (≈5 km) and deep (>10 km) electrical conductivity anomalies beneath Andean volcanoes, Fig. 8 shows the volume fractions of representative melts and saline fluids required to explain the observed anomalies. For the representative melts, we use rhyolitic melt at 800 °C and andesitic melt at 1000 °C (Fig. 7), both assumed to be at water-saturation at the top of each anomaly. We do not consider basaltic melts, as mafic melt reservoirs are more consistent with deeper lower crustal (or uppermost mantle) reservoirs at subduction zones (Hildreth and Moorbath, 1988; Annen et al., 2006). Additionally, although basaltic melts display the highest theoretical electrical conductivities (Fig. 7), the two studied basaltic volcanoes (Villarrica and Osorno) actually exhibit the lowest magnitude electrical conductivity anomalies.

For saline fluids, we use 5 wt% NaCl solution to represent primary magmatic fluids and 40 wt% NaCl solution to represent hypersaline brines. To avoid defining fluid temperatures and pressures, we take the saline fluid electrical conductivities as the peak values in Fig. 3 (34.7 S m^{-1} for 5 wt% NaCl, 187.2 S m^{-1} for 40 wt% NaCl). To calculate the fluid fractions required to generate the observed electrical conductivity anomalies, we assume that the electrical conductivities follow the films mixing model for partial melts (Fig. 6), and that the electrical conductivities are equal to one tenth of the value given by the HS upper bound mixing model for saline fluid fractions <0.15 and follow the tubes mixing model for saline fluid fractions >0.15 (Fig. 4).

Figure 8b shows that water-saturated andesitic melt can explain all of the deep electrical conductivity anomalies except Lastarria, although very high melt fractions (>0.5) are required at Uturuncu and Laguna del Maule. Similarly, water-saturated rhyolitic melt can explain all of the deep anomalies, although a very high melt fraction (≈0.7) is required at Lastarria (the deep electrical conductivity at Lastarria progressively strengthens with depth, which our method does not account for). However, andesitic melt cannot explain the intermediate depth anomalies at six of the eight studied Andean volcanoes (Fig. 8a). As andesite is the typical composition of the studied volcanoes, this casts doubt on the interpretation of the intermediate depth anomalies as partial melt. Furthermore, although moderate fractions of water-saturated rhyolitic melt can explain most of the intermediate depth anomalies, the

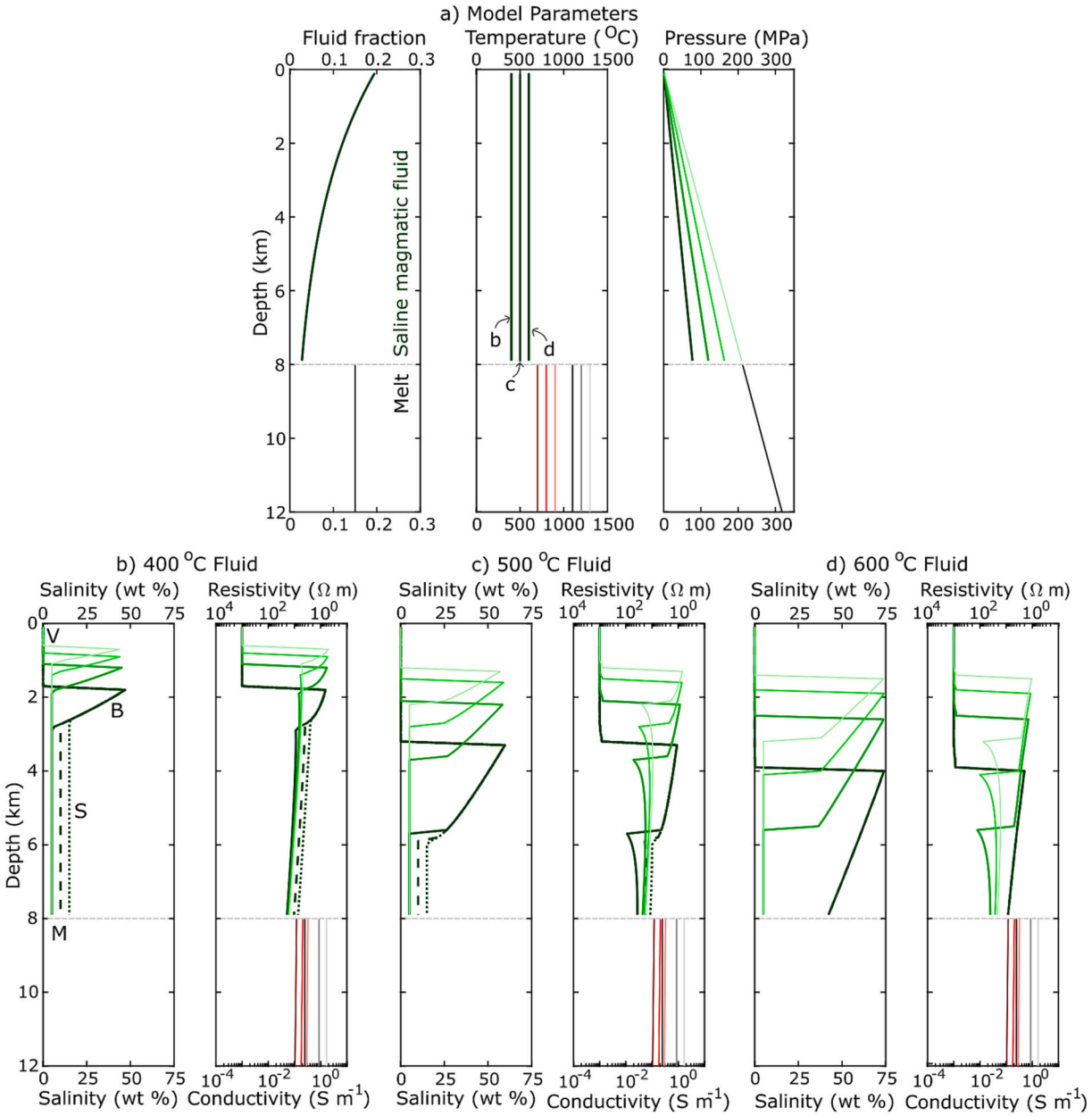

Fig. 9. Simplified models of magmatic systems and their calculated electrical resistivity profiles. The models consist of a lower melt reservoir of basaltic (grey) or rhyolitic (red) composition with 5 wt% water, overlain by an exsolved magmatic fluid column (green). a) Model parameters as a function of depth. Variable magmatic fluid temperatures of 400 °C, 500 °C, and 600 °C correspond to the panels b), c), and d) respectively. Variable fluid pressures from hydrostatic (darkest green) to lithostatic (lightest green) are also shown. b-d) The calculated salinities of the magmatic fluid column and the calculated electrical conductivites of the entire system. The effects of increased bulk magmatic fluid salinities of 10 and 15 wt% NaCl are shown by dashed and dotted lines respectively for the hydrostatic magmatic fluid pressure gradient only. In b), the locations of the domains for the hydrostatic fluid pressure case are indicated for visualisation (M = melt, S = supercritical, B = brine, V = vapour). (For interpretation of the references to colour in this figure legend, the reader is referred to the web version of this article.)

intermediate depth anomalies at Láscar and Laguna del Maule cannot be explained by rhyolitic melt either. Therefore, saline magmatic fluids are the more likely explanation for at least some, if not most, of the intermediate depth electrical conductivity anomalies. Despite using a lower spatial connectivity mixing model, only relatively low saline fluid fractions (<0.2) are required to explain the intermediate depth anomalies. For hypersaline brines, a fluid fraction of <0.05 can explain most of the intermediate depth anomalies, although higher fluid fractions are required at Láscar and Laguna del Maule.

4.2. Electrical resistivity structure of magmatic systems

To further link the laboratory-derived electrical conductivity relationships with the results of magnetotelluric studies at volcanoes, we now present simplified models of magmatic systems and calculate their electrical resistivity structures. Detailed dynamic models of magmatic-hydrothermal systems are provided by Scott et al. (2017) and Afanasyev et al. (2018), but our focus is to investigate the range of electrical resistivity structures beneath volcanoes and identify the main physical controls. Similar models to those presented here were recently published by Watanabe et al. (2022).

In our models (Fig. 9a), we define a partial melt reservoir with 0.15 melt fraction between 8 km depth and the base of the model at 12 km, consistent with the deep electrical conductivity anomalies at Andean volcanoes (Fig. 1). This melt reservoir has a water content of 5 wt%, such that the top of the reservoir is close to water saturation. The melt composition is not important for our results, but we show both basaltic and rhyolitic reservoirs for comparison. Overlying (and derived from) the melt reservoir, magmatic fluids with a bulk salinity of 5–15 wt% NaCl are are assumed to fill the existing porosity structure, which decays exponentially with depth. Our results are not sensitive to the exact porosity structure, but we use similar porosities to Afanasyev et al. (2018) modified to better match the porosity structures observed in volcanic-hosted geothermal reservoirs (e.g. Blundy et al., 2021). In the magmatic fluid column, we apply fluid temperatures from 400 to 600°C and fluid pressure gradients between hydrostatic and lithostatic (i.e. densities between 1000 and 2700 kg m^{-3}) to investigate variations in the depths of phase changes and the effects on the electrical resistivity structure. Where vapour and hypersaline brine phases coexist, we assume that the vapour escapes upwards towards the surface, so the fluid salinity and electrical conductivity are given by the brine phase alone. Where vapour and halite phases coexist, the fluid salinity and electrical conductivity are given by the vapour phase, as halite is not electrically conductive. Finally, to calculate the model electrical resistivity structure, we use the films mixing model for the partial melt (Fig. 6) and take electrical conductivities as equal to one tenth of the value given by the HS upper bound mixing model for the saline magmatic fluids (Fig. 4). We do not attempt to model the formation of a smectite clay layer by hydrothermal reactions at shallow depths.

Figure 9 shows the electrical resistivity profiles generated by our simplified magmatic system models. The models consist of four domains with depth, defined by the fluid phase(s) present and their salinity. The deepest domain is associated with the melt reservoir, with Fig. 9 showing water-saturated basaltic and rhyolitic melts. For these water-saturated melts, the electrical conductivity of the melt domain spans the range of 0.1 to 1 S m^{-1} typical for electrical conductivity anomalies beneath volcanoes. Water under-saturated melts would have lower electrical conductivities. Although appearing as constant in our models, in reality the electrical conductivity of the melt domain would likely decrease towards shallower depths due to water exsolution and decreasing temperature.

Directly overlying the melt reservoir, the magmatic fluid column is usually in a supercritical state and therefore has a salinity equal to that of the initial exsolved magmatic fluid. For particularly hot magmatic fluids under sufficiently low pressures, the supercritical domain may be absent (Fig. 9d). The supercritical fluid domain generally has a relatively low electrical conductivity on the order of 10^{-2} S m^{-1}, occasionally reaching 10^{-1} S m^{-1} for high bulk salinities. Higher magmatic fluid pressures and salinities increase the electrical conductivity of the supercritical domain, whereas higher temperatures decrease the electrical conductivity.

Above the supercritical domain, lower pressure causes the magmatic fluid to separate into hypersaline brine and vapour phases. The high salinity of the brine causes this domain to have an electrical conductivity of generally 0.1 to 1 S m^{-1}, which is typical for electrical conductivity anomalies observed beneath volcanoes. The depth of the brine domain is highly dependent on the pressure and temperature conditions. For greater magmatic fluid temperatures, the brine domain exists over a greater depth range; for fluid temperatures of 300 °C, there is no significant brine lens. Higher fluid pressures shift the brine domain towards shallower depths. In our static models, the initial salinity of the exsolved magmatic fluid has little effect on the brine domain properties.

The electrical conductivity of the magmatic fluid column in the supercritical and brine domains increases towards shallower depths, due to increasing porosity and brine formation. Above the brine domain, further pressure decrease causes a transition to coexisting vapour and halite phases. The vapour domain has negligible electrical conductivity, although clay caps (not modelled here) could generate electrical conductivity anomalies at these depths depending on the temperature and the availability of clay-forming lithologies.

Although simplified, our models produce electrical resistivity profiles that can explain the features revealed by magnetotelluric studies at Andean volcanoes (Fig. 1). For example, colder magmatic fluid temperatures result in a vertically extensive supercritical fluid domain with relatively low electrical conductivity, which separates the shallower electrically conductive brine lens from the deeper electrically conductive melt reservoir (Fig. 9b). Separated intermediate depth and deep anomalies are observed at Uturuncu, Láscar, and Lastarria. By contrast, hotter magmatic fluid temperatures result in a deeper and more vertically extensive brine lens, with less separation between the melt reservoir and the brine domain (Fig. 9d). This may give the appearance of a continuous electrical conductivity anomaly with depth, as seen at Laguna del Maule and Tinguiririca. A continuous anomaly with depth could also occur for colder magmatic fluids with a high bulk salinity (≥10 wt%: Fig. 9a). The melt reservoir depth, fixed in our models at 8 km, is also important in determining whether the intermediate depth and deep anomalies are connected.

Important differences between our models and those of Watanabe et al. (2022) arise from how the electrical conductivities are calculated in the magmatic fluid column. We calculate the electrical conductivities of saline fluids using a value equal to one tenth of that given by the HS upper bound mixing model (Fig. 4). This approach suggests that intermediate depth electrical conductivity anomalies on the order of 0.1 to 1 S m^{-1} are best interpreted as hypersaline brine lenses, as lower salinity primary magmatic fluids generally produce electrical conductivities <0.1 S m^{-1} (Fig. 9). By contrast, Watanabe et al. (2022) use the HS upper bound mixing model, which allows them to explain the intermediate depth anomalies using fluids with a salinity as low as 0.5 wt% NaCl. Additionally, in the brine-vapour coexistence region, Watanabe et al. (2022) calculate the bulk fluid electrical conductivity of the mixed hypersaline brine and vapour phases, whereas we assume that the vapour escapes upwards and we only consider the brine phase (e.g. Afanasyev et al., 2018). Consequently, our electrical conductivities in the brine domain are greater than those of Watanabe et al. (2022).

While both our approach and that of Watanabe et al. (2022) may be valid for different circumstances, we highlight that our approach can explain the observed electrical resistivity structures beneath Andean volcanoes. However, we also recognise other alternative explanations. For example, whether the intermediate depth and deep anomalies are connected could relate to the current volume of fluid transfer between the melt reservoir and the overlying brine lens. Alternatively, depending on their electrical conductivity, some intermediate depth anomalies

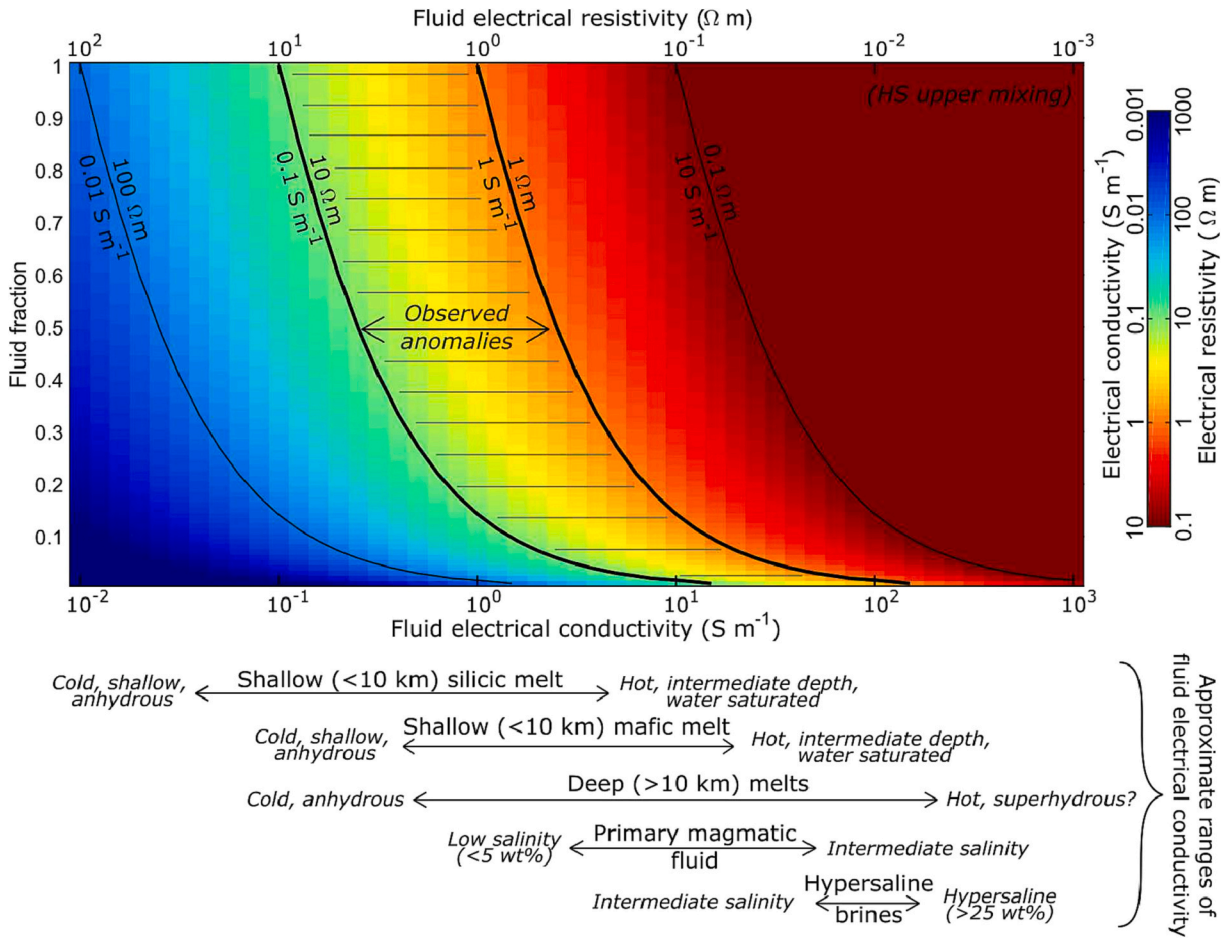

Fig. 10. Electrical conductivities (colour shading) calculated using the HS upper bound (high spatial connectivity) mixing model, as a function of fluid electrical conductivity and fluid fraction. Approximate ranges of fluid electrical conductivities are shown below the chart. The region corresponding to typical observed electrical conductivity anomalies on the order of 0.1 to 1 S m^{-1} is also indicated. Note that extremely high fractions of shallow silicic melt are required to explain typical anomalies, while only very low fractions of hypersaline brines are required (the chosen mixing model is also an important consideration).

could represent shallow melt reservoirs. In this case, the connection between the intermediate depth and deep anomalies would relate to melt transfer between the two reservoirs instead.

5. Discussion

5.1. Interpreting magnetotelluric studies at volcanoes

Magnetotelluric studies reveal a range of electrical resistivity structures beneath Andean volcanoes (Fig. 1). With the exception of shallow electrical conductivity anomalies attributable to clay minerals, interpretation of these anomalies generally aims to ascertain the nature of the causative fluid phase. At the first order, this involves distinguishing between partial melt or saline magmatic fluids, while more detailed analyses may explore factors such as fluid temperature, composition, and fraction. However, we have shown that even the distinction between partial melt and saline magmatic fluids is difficult using magnetotelluric data alone. The exception to this at arc volcanoes are relatively shallow anomalies (<10 km) with high electrical conductivities (≥1 S m^{-1}), which are difficult to explain with partial melt and so most likely represent saline fluids (Fig. 10). The intermediate depth (≈5 km) anomalies beneath Láscar and Laguna del Maule belong to this category, while the intermediate depth anomalies beneath several other Andean volcanoes likely cannot be explained using typical andesitic partial melts (Fig. 8), as is also noted in the original magnetotelluric studies at Paniri, Uturuncu, and Laguna del Maule (Mancini et al., 2019; Comeau et al., 2016; Pearce et al., 2020). Consequently, we generally favour saline magmatic fluids as the source of the intermediate depth anomalies. By contrast, the deep (>10 km) electrical conductivity anomalies at Andean volcanoes are all interpreted as partial melt by the original magnetotelluric studies (Fig. 1); we agree with this view, as the high water solubility in melts at greater depths can explain the high electrical conductivities while also reducing fluid exsolution and the formation of saline magmatic fluids.

5.2. Integrating complementary data

The interpretation of the intermediate depth electrical conductivity anomalies as saline magmatic fluids leads to a model of deeper (>10 km) melt reservoirs, overlain by saline magmatic fluids (≈5 km), and capped by a clay alteration layer (<3 km). In general, this three layer model fits the studied Andean volcanoes well and be can reproduced using simplified magmatic system models (Fig. 9). However, previous magnetotelluric studies often infer the presence of partial melt in the intermediate depth anomalies (Fig. 1). Given the at best ambiguous evidence for intermediate depth partial melt from magnetotelluric data alone, interpretation of partial melt in the intermediate depth anomalies must rely on further information. For the studied Andean volcanoes, the most commonly cited evidence for intermediate depth partial melt comes from geobarometry analyses of erupted products, as cited at Paniri (Cerro del León) Uturuncu, Laguna del Maule, and Villarrica (De Silva et al., 1994; Muir et al., 2014; Klug et al., 2020; Morgado et al., 2015). At

the global scale, both petrologically and geophysically (based mainly on surface deformation and seismic tomography) inferred melt storage depths also cluster around intermediate depths between 4 and 6 km (Rasmussen et al., 2022). Taken together, these observations suggest that partial melt may also be present in the intermediate depth electrical conductivity anomalies, although we favour saline magmatic fluids as the source of the enhanced electrical conductivities.

For the intermediate depth anomalies to represent coexisting melt and saline fluids, the saline fluids must have high spatial connectivity; isolated bubbles of exsolved magmatic fluids within a partial melt will not significantly increase the electrical conductivity. Nonetheless, the coexistence of partial melt and saline magmatic fluids at intermediate depths may not be uncommon, especially over the kilometer scale resolution of volcano geophysical surveys. In the geological record, mixed melt and magmatic fluid systems at intermediate depths are preserved as hydrothermal alteration zones surrounding magmatic intrusions, which in arc environments may also be associated with economic mineralisation to form porphyry copper deposits. In these systems, small (<1 km across) porphyritic dykes derived from a deeper pluton act as sources and pathways for magmatic fluids that produce characteristic halos of alteration and potentially also mineralisation surrounding the intrusion (Sillitoe, 2010). Porphyry emplacement depths, typically in the upper 4 km but up to 9 km depth, match well with the intermediate depth electrical conductivity anomalies, while the underlying parental plutons inferred to be located at 5–15 km depth overlap with the deep electrical conductivity anomalies (Dilles et al., 2000; Cloos, 2001; Singer et al., 2005).

Although the exact nature of the intermediate depth electrical conductivity anomalies remains ambiguous, there exists one instance of an intermediate depth anomaly being directly sampled by drilling. At Kakkonda, Japan, drilling penetrated the fringes of an intermediate depth anomaly at 3.7 km depth, whereupon hypersaline fluid seeped into the well and was recovered by reverse circulation. The fluid had a salinity of 39–55 wt% and temperature of 500 °C, while the host rock porosity was measured as 0.024 (Kasai et al., 1998; Fujimoto et al., 2000). Using these values and assuming that the electrical conductivity

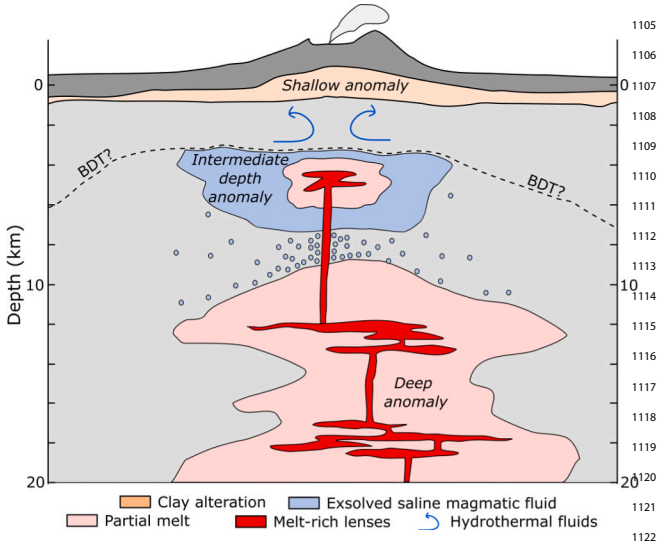

Fig. 11. The generalised model proposed to explain electrical resistivity structures imaged by magnetotelluric studies at Andean volcanoes. Electrical conductivity anomalies at deep (>10 km), intermediate (≈5 km), and shallow (<3 km) depths are consistent with a model of deeper melt reservoirs, overlain by exsolved saline magmatic fluids, and capped by a clay alteration layer. Typical geothermal exploration targets hydrothermal fluids (low electrical conductivity meteoric or sea water) circulating beneath the clay cap but above the brittle-ductile transition (BDT). Interpretation of the deeper structure must therefore rely on indirect imaging such as magnetotelluric surveys.

is equal to one tenth of the value given by the HS upper bound mixing model, as suggested by laboratory data for low porosities (Fig. 4), we obtain an electrical conductivity of 0.16–0.26 S m^{-1}. This is a reasonable match to the electrical conductivity of 0.10–0.16 S m^{-1} in the resistivity model inverted from magnetotelluric data (Uchida et al., 2000). For the same fluid, the central part of the intermediate depth anomaly at Kakkonda with an electrical conductivity of around 1 S m^{-1} requires a fluid fraction of 0.15. However, it is also possible that the saline fluid reservoir at Kakkonda is actually in a supercritical state, and that the hypersaline fluid recovered from the well was formed by phase separation induced by drilling.

5.3. Implications for magmatic systems

The variations in the electrical resistivity structures imaged at Andean volcanoes could reflect differences in the magnetotelluric methodology between studies, the diverse geological characteristics of the volcanoes, or the dynamic nature of magmatic systems. Overall, the imaged electrical conductivity anomalies are consistent with a model consisting of a deep (>10 km) vertically-extensive partially-molten magmatic reservoir, overlain by intermediate depth (≈5 km) exsolved saline magmatic fluids, and finally a shallow clay cap (<3 km) (Fig. 11). The exact nature of the intermediate depth anomalies is unclear; saline magmatic fluids are generally most consistent with the observed electrical conductivities, but localised regions of melt, present at least transiently, cannot be discounted. Therefore, the intermediate depth anomalies likely represent mixed melt and magmatic fluid systems, such as those responsible for forming magmatic-hydrothermal alteration zones and copper porphyry deposits.

The deep electrical conductivity anomalies, which are interpreted as melt reservoirs, are generally vertically-extensive (Fig. 1), consistent with the transcrustal magmatic system model. Furthermore, the intermediate depth and deep anomalies are often connected, providing further evidence for the transcrustal model. However, smoothing and a lack of sensitivity at large depths during inversion can blur the image. By contrast, separated deep and intermediate depth anomalies are consistent with models of a deep melt reservoir periodically supplying melt to a shallower reservoir (Gudmundsson, 2006). Several of the intermediate depth anomalies are dipping, perhaps highlighting the importance of host-rock structures in controlling melt and magmatic fluid pathways. Both the intermediate depth and deep anomalies are also often laterally offset from the volcanic edifices, and recent eruptions do not always occur from the volcano located closest to the imaged reservoirs (e.g. Planchón-Peteroa erupted in 2019, while Tinguiririca last erupted in 1917).

The nature of the intermediate depth anomalies is important from a natural resources perspective for projects aiming to harness high enthalpy geothermal energy or extract metals from saline magmatic fluids. Metal content in magmatic fluids is strongly positively correlated with the fluid salinity (Blundy et al., 2021), but determining fluid salinity from magnetotelluric data alone is challenging. Although our simplified magmatic system models favour hypersaline brines as the cause of the intermediate depth anomalies, they also predict that intermediate depth hypersaline brine lenses should have electrical conductivities on the order of 1 S m^{-1} (Fig. 9). At the studied Andean volcanoes, such strong (≥1 S m^{-1}) intermediate depth anomalies are rare, only being observed at Laguna del Maule and Láscar (Fig. 1). Therefore, large hypersaline brine lenses that represent precursors to potential porphyry copper deposits (Blundy et al., 2015) and prospective targets for extraction of saline magmatic fluids for metal recovery (Blundy et al., 2021) may be relatively rare features (e.g. Stoltnow et al., 2023). The scarcity of very strong (≥1 S m^{-1}) intermediate depth anomalies indicative of large hypersaline brine lenses is also consistent with the rarity of large well-mineralised porphyry copper deposits. Conversely, commonly observed less electrically conductive (0.1 to 1 S m^{-1}) intermediate depth anomalies beneath volcanoes (Fig. 1) may

represent lower salinity or poorly connected saline fluids, consistent with the common occurrence of non- or poorly-mineralised magmatic-hydrothermal alteration zones throughout volcanic arcs (Richards, 2018).

5.4. Future directions

Magnetotelluric studies provide useful insights into the sub-surface structure at volcanoes, although uncertainties remain when interpreting the imaged electrical conductivity anomalies. To constrain these uncertainties, it is important to have accurate laboratory-derived electrical conductivity relationships and an understanding of the appropriate spatial connectivities. Opportunities exist to add to our knowledge in this area. Specifically, it would be useful to have more generalised electrical conductivity relationships for silicate melts, and for these to be constrained at crustal pressures. The electrical conductivity of hypersaline brines also requires further study. Most importantly, more work investigating the geometry and spatial connectivity of melt and fluids depending on pressure, fluid and rock composition, and fluid fraction is needed, especially at low fluid fractions and in crystalline rocks. Extending these relationships to three or more phases (e.g. host rock ± melt ± fluid ± sulphide) and investigating the coexistence of phases (e.g. brine + vapour) could also help with the interpretation of magnetotelluric data.

To best employ laboratory-derived electrical conductivity relationships, analyses at individual volcanoes should incorporate petrological constraints. For example, the low electrical conductivities observed at Osorno are thought to arise from the very low water contents in the melts (Tagiri et al., 1993), which reduces the melt electrical conductivity and limits magmatic fluid exsolution. However, a single volcano may exhibit several different melt compositions, and petrologically inferred melt storage temperatures can vary by several hundred degrees (e.g. Boschetty et al., 2022). Furthermore, whether the spatial connectivity determined in the laboratory is applicable to transcrustal scale magnetotelluric surveys is also an important consideration. For example, localised well-connected melt-rich lenses within lower melt fraction mushes may be present at scales below the resolution of the magnetotelluric survey, which would have the effect of smoothing out the imaged electrical conductivity anomaly.

Our review of magnetotelluric investigations at Andean volcanoes could also be expanded to cover other areas and tectonic settings. At other subduction zones, magnetotelluric studies at volcanoes are generally consistent with the findings from the Andes. For example, spatially separate intermediate depth and deep electrical conductivity anomalies have been imaged beneath volcanoes in New Zealand (Bertrand et al., 2012), North America (Peacock et al., 2016), and Japan (Aizawa et al., 2022), while other subduction zone volcanoes display a single vertically-extensive electrical conductivity anomaly (e.g. Hill et al., 2009; Aizawa et al., 2014; Ogawa et al., 2014; Matsushima et al., 2020). By contrast, rift or hotspot volcanoes likely have hotter more mafic melt compositions but much lower water contents than arc volcanoes, which may produce different electrical resistivity structures.

6. Conclusions

The commonly observed electrical resistivity structure beneath Andean arc volcanoes of deep (>10 km), intermediate depth (≈5 km), and shallow (<3 km) electrical conductivity anomalies is consistent with a model of deeper melt reservoirs, overlain by saline magmatic fluids, and capped by a clay alteration layer (Fig. 11). Although many previous studies attribute the intermediate depth anomalies to the presence of partial melt, we show that saline magmatic fluids are generally more consistent with the observed electrical conductivities. However, the presence of partial melt at intermediate depths is also likely, suggesting that the intermediate depth anomalies may represent mixed melt and magmatic fluid systems, such as those responsible for forming magmatic-hydrothermal alteration zones and copper porphyry deposits. Incorporating other petrological and geophysical data, ideally through joint inversion methods, is therefore key for improving the interpretation of magnetotelluric data and understanding the resources and/or hazards potential of magmatic systems. Developments in laboratory-derived electrical conductivity relationships, especially investigating the spatial connectivity of partial melt and saline fluids in the upper crust, are also required to further constrain the interpretation of magnetotelluric studies at volcanoes.

CRediT authorship contribution statement

A.P. Jenkins: Conceptualization, Methodology, Formal analysis, Writing – original draft, Writing – review & editing. **A.C. Rust:** Conceptualization, Methodology, Writing – review & editing. **J. Blundy:** Conceptualization, Methodology, Writing – review & editing. **J. Biggs:** Methodology, Writing – review & editing.

Declaration of Competing Interest

The authors declare that they have no known competing financial interests or personal relationships that could have appeared to influence the work reported in this paper.

Data availability

The original magnetotelluric studies at the eight Andean volcanoes are available from the sources cited in the text. The laboratory-derived electrical conductivity relationships are available from the sources cited in Tables 2 and 3.

Acknowledgements

This work was supported by the Natural Environment Research Council [NE/L002434/1]. A. Jenkins, A. Rust, and J. Blundy were partially supported by BHP. A. Jenkins and J. Biggs were supported by the NERC Centre for the Observation and Modeling of Earthquakes, Volcanoes and Tectonics (COMET: http://comet.nerc.ac.uk), a partnership between UK Universities and the British Geological Survey. J. Biggs and A. Rust received funding from the European Research Council (ERC) under the European Union's Horizon 2020 research and innovation programme (MAST: grant agreement No. 101003173). J. Blundy acknowledges a Royal Society Research Professorship (RP\R1\201048). A. Jenkins and A. Rust attended the IMPROVE/NordVulk summer school on geothermal and magmatic systems held in Iceland during June 2022, which helped to develop the ideas presented here. Helpful and constructive reviews by Martyn Unsworth and an anonymous reviewer improved the original manuscript.

Appendix A. Supplementary data

Supplementary data to this article can be found online at https://doi.org/10.1016/j.jvolgeores.2023.107852.

References

Afanasyev, A., Blundy, J., Melnik, O., Sparks, S., 2018. Formation of magmatic brine lenses via focussed fluid-flow beneath volcanoes. Earth Planet. Sci. Lett. 486, 119–128. https://doi.org/10.1016/j.epsl.2018.01.013.

Aizawa, K., Koyama, T., Hase, H., Uyeshima, M., Kanda, W., Utsugi, M., Yoshimura, R., Yamaya, Y., Hashimoto, T., Yamazaki, K., et al., 2014. Three-dimensional resistivity structure and magma plumbing system of the Kirishima Volcanoes as inferred from broadband magnetotelluric data. J. Geophys. Res. Solid Earth 119, 198–215. https://doi.org/10.1002/2013JB010682.

Aizawa, K., Utsugi, M., Kitamura, K., Koyama, T., Uyeshima, M., Matsushima, N., Takakura, S., Inagaki, H., Saito, H., Fujimitsu, Y., 2022. Magmatic fluid pathways in the upper crust: insights from dense magnetotelluric observations around the Kuju Volcanoes, Japan. Geophys. J. Int. 228, 755–772. https://doi.org/10.1093/gji/ggab368.

Annen, C., Blundy, J., Sparks, R., 2006. The genesis of intermediate and silicic magmas in deep crustal hot zones. J. Petrol. 47, 505–539. https://doi.org/10.1093/petrology/egi084.
Audétat, A., Edmonds, M., 2020. Magmatic-hydrothermal fluids. Elements: an International Magazine of Mineralogy. Geochem. Petrol. 16, 401–406. https://doi.org/10.2138/gselements.16.6.401.
Bachmann, O., Huber, C., 2016. Silicic magma reservoirs in the earth's crust. Am. Mineral. 101, 2377–2404. https://doi.org/10.2138/am-2016-5675.
Bai, T., Thurber, C., Lanza, F., Singer, B., Bennington, N., Keranen, K., Cardona, C., 2020. Teleseismic tomography of the Laguna del Maule volcanic field in Chile. J. Geophys. Res. Solid Earth 125. https://doi.org/10.1029/2020JB019449 e2020JB019449.
Beaufort, D., Rigault, C., Billon, S., Billault, V., Inoue, A., Inoué, S., Patrier, P., Ferrage, E., 2015. Chlorite and chloritization processes through mixed-layer mineral series in low-temperature geological systems - a review. Clay Miner. 50, 497–523. https://doi.org/10.1180/claymin.2015.050.4.06.
Becerril, L., Galindo, I., Gudmundsson, A., Morales, J., 2013. Depth of origin of magma in eruptions. Sci. Rep. 3, 1–6. https://doi.org/10.1038/srep02762.
Bertrand, E., Caldwell, T., Hill, G., Wallin, E., Bennie, S., Cozens, N., Onacha, S., Ryan, G., Walter, C., Zaino, A., et al., 2012. Magnetotelluric imaging of upper-crustal convection plumes beneath the Taupo Volcanic Zone, New Zealand. Geophys. Res. Lett. 39 https://doi.org/10.1029/2011GL050177.
Blundy, J., Mavrogenes, J., Tattitch, B., Sparks, S., Gilmer, A., 2015. Generation of porphyry copper deposits by gas–brine reaction in volcanic arcs. Nat. Geosci. 8, 235–240. https://doi.org/10.1038/ngeo2351.
Blundy, J., Afanasyev, A., Tattitch, B., Sparks, S., Melnik, O., Utkin, I., Rust, A., 2021. The economic potential of metalliferous sub-volcanic brines. R. Soc. Open Sci. 8, 202192 https://doi.org/10.1098/rsos.202192.
Boschetty, F., Ferguson, D., Cortés, J., Morgado, E., Ebmeier, S., Morgan, D., Romero, J., Silva Parejas, C., 2022. Insights into magma storage beneath a frequently erupting arc volcano (Villarrica, Chile) from unsupervised machine learning analysis of mineral compositions. Geochem. Geophys. Geosyst. 23 https://doi.org/10.1029/2022GC010333 e2022GC010333.
Cashman, K., Sparks, R., Blundy, J., 2017. Vertically extensive and unstable magmatic systems: a unified view of igneous processes. Science 355. https://doi.org/10.1126/science.aag3055 eaag3055.
Chaussard, E., Amelung, F., 2014. Regional controls on magma ascent and storage in volcanic arcs. Geochem. Geophys. Geosyst. 15, 1407–1418. https://doi.org/10.1002/2013GC005216.
Chave, A., Jones, A., 2012. The Magnetotelluric Method: Theory and Practice. Cambridge University Press. https://doi.org/10.1017/CBO9781139020138.
Chmielowski, J., Zandt, G., Haberland, C., 1999. The central Andean Altiplano-Puna magma body. Geophys. Res. Lett. 26, 783–786. https://doi.org/10.1029/1999GL900078.
Cloos, M., 2001. Bubbling magma chambers, cupolas, and porphyry copper deposits. Int. Geol. Rev. 43, 285–311. https://doi.org/10.1080/00206810109465015.
Comeau, M., Unsworth, M., Cordell, D., 2016. New constraints on the magma distribution and composition beneath Volcán Uturuncu and the southern Bolivian Altiplano from magnetotelluric data. Geosphere 12, 1391–1421. https://doi.org/10.1130/GES01277.1.
Cooper, K., 2017. What does a magma reservoir look like? The "Crystal's-Eye" view. Elements 13, 23–28. https://doi.org/10.2113/gselements.13.1.23.
Cooper, K., 2019. Time scales and temperatures of crystal storage in magma reservoirs: implications for magma reservoir dynamics. Phil. Trans. R. Soc. A 377, 20180009. https://doi.org/10.1098/rsta.2018.0009.
Cordell, D., Unsworth, M., Daíz, D., 2018. Imaging the Laguna del Maule Volcanic Field, Central Chile using magnetotellurics: evidence for crustal melt regions laterally-offset from surface vents and lava flows. Earth Planet. Sci. Lett. 488, 168–180. https://doi.org/10.1016/j.epsl.2018.01.007.
Cordell, D., Unsworth, M., Lee, B., Daíz, D., Bennington, N., Thurber, C., 2020. Integrating magnetotelluric and seismic images of silicic magma systems: a case study from the Laguna del Maule Volcanic Field, Central Chile. J. Geophys. Res. Solid Earth 125. https://doi.org/10.1029/2020JB020459 e2020JB020459.
Cordell, D., Hill, G., Bachmann, O., Moorkamp, M., Huber, C., 2022. Estimating melt fraction in silicic systems using Bayesian inversion of magnetotelluric data. J. Volcanol. Geotherm. Res. 423, 107470 https://doi.org/10.1016/j.jvolgeores.2022.107470.
Daines, M., Pec, M., 2015. Migration of melt. In: Sigursson, H. (Ed.), The Encyclopedia of Volcanoes. Elsevier, pp. 49–64. https://doi.org/10.1016/B978-0-12-385938-9.00002-X.
Díaz, D., Brasse, H., Ticona, F., 2012. Conductivity distribution beneath Lascar volcano (Northern Chile) and the Puna, inferred from magnetotelluric data. J. Volcanol. Geotherm. Res. 217, 21–29. https://doi.org/10.1016/j.jvolgeores.2011.12.007.
Díaz, D., Heise, W., Zamudio, F., 2015. Three-dimensional resistivity image of the magmatic system beneath Lastarria volcano and evidence for magmatic intrusion in the back arc (northern Chile). Geophys. Res. Lett. 42, 5212–5218. https://doi.org/10.1002/2015GL064426.
Díaz, D., Zúñiga, F., Castruccio, A., 2020. The interaction between active crustal faults and volcanism: a case study of the Liquiñe-Ofqui Fault Zone and Osorno volcano, southern Andes, using magnetotellurics. J. Volcanol. Geotherm. Res. 393, 106806 https://doi.org/10.1016/j.jvolgeores.2020.106806.
De Silva, S., Self, S., Francis, P., Drake, R., Carlos, R., 1994. Effusive silicic volcanism in the Central Andes: the Chao dacite and other young lavas of the Altiplano-Puna Volcanic complex. J. Geophys. Res. Solid Earth 99, 17805–17825. https://doi.org/10.1029/94JB00652.
Dilles, J., Einaudi, M., Proffett, J., Barton, M., 2000. Overview of the Yerington Porphyry Copper District: Magmatic to Nonmagmatic sources of Hydrothermal Fluids, their Flow Paths, Alteration Affects on Rocks, and Cu-Mo-Fe-Au Ores, in: part I. Contrasting styles of intrusion-associated hydrothermal systems. Soc. Econ. Geol. https://doi.org/10.5382/GB.32.
Driesner, T., Heinrich, C., 2007. The system H2O-NaCl. Part I: Correlation formulae for phase relations in temperature-pressure-composition space from 0 to 1000 C, 0 to 5000 bar, and 0 to 1 XNaCl. Geochim. Cosmochim. Acta 71, 4880–4901. https://doi.org/10.1016/j.gca.2006.01.033.
Edmonds, M., Woods, A., 2018. Exsolved volatiles in magma reservoirs. J. Volcanol. Geotherm. Res. 368, 13–30. https://doi.org/10.1016/j.jvolgeores.2018.10.018.
Edmonds, M., Cashman, K., Holness, M., Jackson, M., 2019. Architecture and dynamics of magma reservoirs. Phil. Trans. R. Soc. A 377. https://doi.org/10.1098/rsta.2018.0298, 20180298.
Elders, W., Fridleifsson, G., Albertsson, A., 2014. Drilling into magma and the implications of the Iceland Deep Drilling Project (IDDP) for high-temperature geothermal systems worldwide. Geothermics 49, 111–118. https://doi.org/10.1016/j.geothermics.2013.05.001.
Feigl, K., Le Mével, H., A.S., T, Córdova, L., Andersen, N., DeMets, C., Singer, B., 2014. Rapid uplift in Laguna del Maule volcanic field of the Andean Southern Volcanic zone (Chile) 2007-2012. Geophys. J. Int. 196, 885–901. https://doi.org/10.1093/gji/ggt438.
Fournier, R., 1999. Hydrothermal processes related to movement of fluid from plastic into brittle rock in the magmatic-epithermal environment. Econ. Geol. 94, 1193–1211. https://doi.org/10.2113/gsecongeo.94.8.1193.
Fujimoto, K., Takahashi, M., Doi, N., Kato, O., 2000. High permeability of Quaternary granites in the Kakkonda geothermal area, Northeast Japan. In: World Geothermal Congress. Kyushu-Tohoku, Japan, pp. 1139–1144.
Gaillard, F., 2004. Laboratory measurements of electrical conductivity of hydrous and dry silicic melts under pressure. Earth Planet. Sci. Lett. 218, 215–228. https://doi.org/10.1016/S0012-821X(03)00639-3.
Ghiorso, M., Gualda, G., 2015. An H2O-CO2 mixed fluid saturation model compatible with rhyolite-MELTS. Contrib. Mineral. Petrol. 169, 1–30. https://doi.org/10.1007/s00410-015-1141-8.
Glover, P., 1996. Graphite and electrical conductivity in the lower continental crust: a review. Phys. Chem. Earth 21, 279–287.
Glover, P., Hole, M., Pous, J., 2000. A modified Archie's law for two conducting phases. Earth Planet. Sci. Lett. 180, 369–383. https://doi.org/10.1016/S0012-821X(00)00168-0.
Godoy, B., Lazcano, J., Rodríguez, I., Martínez, P., Parada, M., Le Roux, P., Wilke, H.G., Polanco, E., 2018. Geological evolution of Paniri volcano, Central Andes, northern Chile. J. S. Am. Earth Sci. 84, 184–200. https://doi.org/10.1016/j.jsames.2018.03.013.
Goltz, A., Krawczynski, M., Gavrilenko, M., Gorbach, N., Ruprecht, P., 2020. Evidence for superhydrous primitive arc magmas from mafic enclaves at Shiveluch volcano, Kamchatka. Contrib. Mineral. Petrol. 175, 1–26. https://doi.org/10.1007/s00410-020-01746-5.
Gomez, C., Dvorkin, J., Vanorio, T., 2010. Laboratory measurements of porosity, permeability, resistivity, and velocity on Fontainebleau sandstones. Geophysics 75, E191–E204. https://doi.org/10.1190/1.3493633.
Grant, F., West, G., 1965. Interpretation Theory in Applied Geophysics. McGraw-Hill.
ten Grotenhuis, S., Drury, M., Spiers, C., Peach, C., 2005. Melt distribution in olivine rocks based on electrical conductivity measurements. J. Geophys. Res. Solid Earth 110. https://doi.org/10.1029/2004JB003462.
Gualda, G., Ghiorso, M., 2015. MELTS _ Excel: a Microsoft Excel-based MELTS interface for research and teaching of magma properties and evolution. Geochem. Geophys. Geosyst. 16, 315–324. https://doi.org/10.1002/2014GC005545.
Gudmundsson, A., 2006. How local stresses control magma-chamber ruptures, dyke injections, and eruptions in composite volcanoes. Earth Sci. Rev. 79, 1–31. https://doi.org/10.1016/j.earscirev.2006.06.006.
Guéguen, Y., Palciauskas, V., 1994. Introduction to the Physics of Rocks. Princeton University Press.
Guo, X., Zhang, L., Behrens, H., Ni, H., 2016. Probing the status of felsic magma reservoirs: Constraints from the P-T-H2O dependences of electrical conductivity of rhyolitic melt. Earth Planet. Sci. Lett. 433, 54–62. https://doi.org/10.1016/j.epsl.2015.10.036.
Guo, X., Li, B., Ni, H., Mao, Z., 2017. Electrical conductivity of hydrous andesitic melts pertinent to subduction zones. J. Geophys. Res. Solid Earth 122, 1777–1788. https://doi.org/10.1002/2016JB013524.
Han, T., Best, A., Sothcott, J., North, L., MacGregor, L., 2015. Relationships among low frequency (2 Hz) electrical resistivity, porosity, clay content and permeability in reservoir sandstones. J. Appl. Geophys. 112, 279–289. https://doi.org/10.1016/j.jappgeo.2014.12.006.
Hashin, Z., Shtrikman, S., 1962. A variational approach to the theory of the effective magnetic permeability of multiphase materials. J. Appl. Phys. 33, 3125–3131. https://doi.org/10.1063/1.1728579.
Heinrich, C., 2005. The physical and chemical evolution of low-salinity magmatic fluids at the porphyry to epithermal transition: a thermodynamic study. Mineral. Deposita 39, 864–889. https://doi.org/10.1007/s00126-004-0461-9.
Hildreth, W., Moorbath, S., 1988. Crustal contribtuions to arc magmatism in the Andes of Central Chile. Contrib. Mineral. Petrol. 98, 455–489. https://doi.org/10.1007/BF00372365.
Hill, G., Caldwell, T., Heise, W., Chertkoff, D., Bibby, H., Burgess, M., Cull, J., Cas, R., 2009. Distribution of melt beneath Mount St Helens and Mount Adams inferred from magnetotelluric data. Nat. Geosci. 2, 785–789. https://doi.org/10.1038/ngeo661.
Iacovino, Matthews, Wieser, Moore, Bàuà Iacovino, K., Matthews, S., Wieser, P., Moore, G., Bégué, F., 2021. VESIcal Part I: an open-source thermodynamic model

engine for mixed volatile (H2O-CO2) solubility in silicate melts. Earth and Space. Science 8. https://doi.org/10.1029/2020EA001584 e2020EA001584.
Jay, J., Pritchard, M., West, M., Christensen, D., Haney, M., Minaya, E., Sunagua, M., McNutt, S., Zabala, M., 2012. Shallow seismicity, triggered seismicity, and ambient noise tomography at the long-dormant Uturuncu Volcano, Bolivia. Bull. Volcanol. 74, 817–837. https://doi.org/10.1007/s00445-011-0568-7.
Kasai, K., Sakagawa, Y., Komatsu, R., Sasaki, M., Akaku, K., Uchida, T., 1998. The origin of hypersaline liquid in the Quaternary Kakkonda granite, sampled from well WD-1a, Kakkonda geothermal system, Japan. Geothermics 27, 631–645. https://doi.org/10.1016/S0375-6505(98)00037-6.
Kesler, S., Bodnar, R., Mernagh, T., 2013. Role of fluid and melt inclusion studies in geologic research. Geofluids 13, 398–404. https://doi.org/10.1111/gfl.12055.
Klug, J., Singer, B., Kita, N., Spicuzza, M., 2020. Storage and evolution of Laguna del Maule rhyolites: insight from volatile and trace element contents in melt inclusions. J. Geophys. Res.: SolidEarth 125. https://doi.org/10.1029/2020JB019475 e2020JB019475.
Krawczynski, M., Grove, T., Behrens, H., 2012. Amphibole stability in primitive arc magmas: effects of temperature, H2O content, and oxygen fugacity. Contrib. Mineral. Petrol. 164, 317–339. https://doi.org/10.1007/s00410-012-0740-x.
Kruszewski, M., Wittig, V., 2018. Review of failure modes in supercritical geothermal drilling projects. Geothermal Energy 6, 1–29. https://doi.org/10.1186/s40517-018-0113-4.
Laštovičková, M., 1991. A review of laboratory measurements of the electrical conductivity of rocks and minerals. Phys. Earth Planet. Inter. 66, 1–11. https://doi.org/10.1016/0031-9201(91)90099-4.
Laumonier, M., Gaillard, F., Sifre, D., 2015. The effect of pressure and water concentration on the electrical conductivity of dacitic melts: Implication for magnetotelluric imaging in subduction areas. Chem. Geol. 418, 66–76. https://doi.org/10.1016/j.chemgeo.2014.09.019.
Laumonier, M., Gaillard, F., Muir, D., Blundy, J., Unsworth, M., 2017. Giant magmatic water reservoirs at mid-crustal depth inferred from electrical conductivity and the growth of the continental crust. Earth Planet. Sci. Lett. 457, 173–180. https://doi.org/10.1016/j.epsl.2016.10.023.
Lee, B., Unsworth, M., Árnason, K., Cordell, D., 2020. Imaging the magmatic system beneath the Krafla geothermal field, Iceland: a new 3-D electrical resistivity model from inversion of magnetotelluric data. Geophys. J. Int. 220, 541–567. https://doi.org/10.1093/gji/ggz427.
Lesher, C., Spera, F., 2015. Thermodynamic and transport properties of silicate melts and magma. In: The Encyclopedia of Volcanoes. Elsevier, pp. 113–141. https://doi.org/10.1016/B978-0-12-385938-9.00005-5.
Magee, C., Stevenson, C., Ebmeier, S., Keir, D., Hammond, J., Gottsmann, J., Whaler, K., Schofield, N., Jackson, C., Petronis, M., et al., 2018. Magma plumbing systems: a geophysical perspective. J. Petrol. 59, 1217–1251. https://doi.org/10.1093/petrology/egy064.
Mancini, R., Daíz, D., Brasse, H., Godoy, B., Hernández, M., 2019. Conductivity distribution beneath the San Pedro-Linzor volcanic chain, North Chile, using 3-D magnetotelluric modeling. J. Geophys. Res. Solid Earth 124, 4386–4398. https://doi.org/10.1029/2018JB016114.
Matsushima, N., Utsugi, M., Takakura, S., Yamasaki, T., Hata, M., Hashimoto, T., Uyeshima, M., 2020. Magmatic–hydrothermal system of Aso Volcano, Japan, inferred from electrical resistivity structures. Earth Planets Space 72, 1–20. https://doi.org/10.1186/s40623-020-01180-8.
Miller, C., Williams-Jones, G., Fournier, D., Witter, J., 2017. 3D gravity inversion and thermodynamic modelling reveal properties of shallow silicic magma reservoir beneath Laguna del Maule, Chile. Earth Planet. Sci. Lett. 459, 14–27. https://doi.org/10.1016/j.epsl.2016.11.007.
Mora-Stock, C., 2015. Seismic Structure and Seismicity of the Villarrica Volcano (Southern Central Chile). Ph.D. thesis.. Christian-Albrechts-Universität.
Morgado, E., Parada, M., Contreras, C., Castruccio, A., Gutiérrez, F., McGee, L., 2015. Contrasting records from mantle to surface of Holocene lavas of two nearby arc volcanic complexes: Caburgua-Huelemolle Small Eruptive Centers and Villarrica Volcano, Southern Chile. J. Volcanol. Geotherm. Res. 306, 1–16. https://doi.org/10.1016/j.jvolgeores.2015.09.023.
Muir, D., Blundy, J., Rust, A., Hickey, J., 2014. Experimental constraints on dacite pre-eruptive magma storage conditions beneath Uturuncu volcano. J. Petrol. 55, 749–767. https://doi.org/10.1093/petrology/egu005.
Müntener, O., Ulmer, P., Blundy, J., 2021. Superhydrous arc magmas in the alpine context. Elements 17, 35–40. https://doi.org/10.2138/gselements.17.1.35.
Ni, H., Keppler, H., Behrens, H., 2011. Electrical conductivity of hydrous basaltic melts: implications for partial melting in the upper mantle. Contrib. Mineral. Petrol. 162, 637–650. https://doi.org/10.1007/s00410-011-0617-4.
Ni, H., Chen, Q., Keppler, H., 2014. Electrical conductivity measurements of aqueous fluids under pressure with a hydrothermal diamond anvil cell. Rev. Sci. Instrum. 85, 115107 https://doi.org/10.1063/1.4902152.
Ogawa, Y., Ichiki, M., Kanda, W., Mishina, M., Asamori, K., 2014. Three-dimensional magnetotelluric imaging of crustal fluids and seismicity around Naruko volcano, NE Japan. Earth Planets Space 66, 1–13. https://doi.org/10.1186/s40623-014-0158-y.
Pavez, C., Tapia, F., Comte, D., Gutierrez, F., Lira, E., Charrier, R., Benavente, O., 2016. Characterization of the hydrothermal system of the Tinguiririca Volcanic complex, Central Chile, using structural geology and passive seismic tomography. J. Volcanol. Geotherm. Res. 310, 107–117. https://doi.org/10.1016/j.jvolgeores.2015.11.018.
Pavez, M., Schill, E., Held, S., Daíz, D., Kohl, T., 2020. Visualizing preferential magmatic and geothermal fluid pathways via electric conductivity at Villarrica Volcano, S-Chile. J. Volcanol. Geotherm. Res. 400, 106913 https://doi.org/10.1016/j.jvolgeores.2020.106913.
Peacock, J., Mangan, M., McPhee, D., Wannamaker, P., 2016. Three-dimensional electrical resistivity model of the hydrothermal system in Long Valley Caldera, California, from magnetotellurics. Geophys. Res. Lett. 43, 7953–7962. https://doi.org/10.1002/2016GL069263.
Pearce, R., Sánchez de la Muela, A., Moorkamp, M., Hammond, J., Mitchell, T., Cembrano, J., Araya Vargas, J., Meredith, P., Iturrieta, P., Pérez-Estay, N., et al., 2020. Reactivation of fault systems by compartmentalized hydrothermal fluids in the Southern Andes revealed by magnetotelluric and seismic data. Tectonics 39. https://doi.org/10.1029/2019TC005997 e2019TC005997.
Piña-Varas, P., Ledo, J., Queralt, P., Marcuello, A., Perez, N., 2018. On the detectability of Teide volcano magma chambers (Tenerife, Canary Islands) with magnetotelluric data. Earth Planets Space 70, 1–11. https://doi.org/10.1186/s40623-018-0783-y.
Pommier, A., Le-Trong, E., 2011. "SIGMELTS": a web portal for electrical conductivity calculations in geosciences. Comput. Geosci. 37, 1450–1459. https://doi.org/10.1016/j.cageo.2011.01.002.
Pritchard, M., De Silva, S., Michelfelder, G., Zandt, G., McNutt, S., Gottsmann, J., West, M., Blundy, J., Christensen, D., Finnegan, N., et al., 2018. Synthesis: PLUTONS: investigating the relationship between pluton growth and volcanism in the Central Andes. Geosphere 14, 954–982. https://doi.org/10.1130/GES01578.1.
Quist, A., Marshall, W., 1968. Electrical conductances of aqueous sodium chloride solutions from 0 to 800. degree. and at pressures to 4000 bars. J. Phys. Chem. 72, 684–703. https://doi.org/10.1021/j100848a050.
Rasmussen, D., Plank, T., Roman, D., Zimmer, M., 2022. Magmatic water content controls the pre-eruptive depth of arc magmas. Science 375, 1169–1172. https://doi.org/10.1126/science.abm5174.
Reinsch, T., Dobson, P., Asanuma, H., Huenges, E., Poletto, F., Sanjuan, B., 2017. Utilizing supercritical geothermal systems: a review of past ventures and ongoing research activities. Geothermal Energy 5, 1–25. https://doi.org/10.1186/s40517-017-0075-y.
Richards, J.P., 2018. A shake-up in the porphyry world? Econ. Geol. 113 (6), 1225–1233.
Rosenberg, C., Handy, M., 2005. Experimental deformation of partially melted granite revisited: implications for the continental crust. J. Metamorph. Geol. 23, 19–28. https://doi.org/10.1111/j.1525-1314.2005.00555.x.
Ryan, G., Peacock, J., Shalev, E., Rugis, J., 2013. Montserrat geothermal system: a 3D conceptual model. Geophys. Res. Lett. 40, 2038–2043. https://doi.org/10.1002/grl.50489.
Samrock, F., Grayver, A., Bachmann, O., Karakas, Ö., Saar, M., 2021. Integrated magnetotelluric and petrological analysis of felsic magma reservoirs: Insights from Ethiopian rift volcanoes. Earth Planet. Sci. Lett. 559, 116765 https://doi.org/10.1016/j.epsl.2021.116765.
Scott, S., Driesner, T., Weis, P., 2017. Boiling and condensation of saline geothermal fluids above magmatic intrusions. Geophys. Res. Lett. 44, 1696–1705. https://doi.org/10.1002/2016GL071891.
Sillitoe, R.H., 2010. Porphyry Copper Systems. Econ. Geol. 105, 3–41. https://doi.org/10.2113/gsecongeo.105.1.3.
Simpson, F., Bahr, K., 2005. Practical Magnetotellurics. Cambridge University Press. https://doi.org/10.1017/CBO9780511614095.
Singer, D., Berger, V., Moring, B., 2005. Porphyry Copper Deposits of the World: Database, Maps, Grade and Tonnage Models. US Department of the Interior, US Geological Survey Reston doi: http://pubs.usgs.gov/of/2005/1060/.
Sinmyo, R., Keppler, H., 2017. Electrical conductivity of NaCl-bearing aqueous fluids to 600 C and 1 GPa. Contrib. Mineral. Petrol. 172, 1–12. https://doi.org/10.1007/s00410-016-1323-z.
Sparks, R., Folkes, C., Humphreys, M., Barfod, D., Clavero, J., Sunagua, M., McNutt, S., Pritchard, M., 2008. Uturuncu volcano, Bolivia: Volcanic unrest due to mid-crustal magma intrusion. Am. J. Sci. 308, 727–769. https://doi.org/10.2475/06.2008.01.
Sparks, R.S.J., Cashman, K.V., 2017. Dynamic magma systems: implications for forecasting volcanic activity. Elements 13, 35–40. https://doi.org/10.2113/gselements.13.1.35.
Sparks, R.S.J., Annen, C., Blundy, J., Cashman, K.V., Rust, A., Jackson, M., 2019. Formation and dynamics of magma reservoirs. Phil. Trans. R. Soc. A 377, 20180019. https://doi.org/10.1098/rsta.2018.0019.
Spica, Z., Legrand, D., Iglesias, A., Walter, T., Heimann, S., Dahm, T., Froger, J.L., Rémy, D., Bonvalot, S., West, M., et al., 2015. Hydrothermal and magmatic reservoirs at Lazufre volcanic area, revealed by a high-resolution seismic noise tomography. Earth Planet. Sci. Lett. 421, 27–38. https://doi.org/10.1016/j.epsl.2015.03.042.
Stimac, J., Goff, F., Goff, C., 2015. Intrusion-related geothermal systems. In: The Encyclopedia of Volcanoes. Elsevier, pp. 799–822. https://doi.org/10.1016/B978-0-12-385938-9.00046-8.
Stoltnow, M., Weis, P., Korges, M., 2023. Hydrological controls on base metal precipitation and zoning at the porphyry-epithermal transition constrained by numerical modeling. Sci. Rep. 13, 3786. https://doi.org/10.1038/s41598-023-30572-5.
Tagiri, M., Moreno, H., Lṕpez-Escobar, L., Notsu, K., 1993. Two magma types of the high-alumina basalt series of Osorno Volcano, Southern Andes (41 06 S) - plagioclase dilution effect. J. Mineral. Petrol. Econ. Geol. 88, 359–371. https://doi.org/10.2465/ganko.88.359.
Tattitch, B., Chelle-Michou, C., Blundy, J., Loucks, R., 2021. Chemical feedbacks during magma degassing control chlorine partitioning and metal extraction in volcanic arcs. Nat. Commun. 12, 1–11. https://doi.org/10.1038/s41467-021-21887-w.
Uchida, T., Ogawa, Y., Takakura, S., Mitsuhata, Y., 2000. Geoelectrical investigation of the Kakkonda geothermal field, northern Japan. In: Proceedings World Geothemal Congress. Tohoku-Kyushu, Japan, pp. 1893–1898.

Vigneresse, J., Barbey, P., Cuney, M., 1996. Rheological transitions during partial melting and crystallization with application to felsic magma segregation and transfer. J. Petrol. 37, 1579–1600. https://doi.org/10.1093/petrology/37.6.1579.

Waff, H., 1974. Theoretical considerations of electrical conductivity in a partially molten mantle and implications for geothermometry. J. Geophys. Res. 79, 4003–4010. https://doi.org/10.1029/JB079i026p04003.

Ward, K., Zandt, G., Beck, S., Christensen, D., McFarlin, H., 2014. Seismic imaging of the magmatic underpinnings beneath the Altiplano-Puna volcanic complex from the joint inversion of surface wave dispersion and receiver functions. Earth Planet. Sci. Lett. 404, 43–53. https://doi.org/10.1016/j.epsl.2014.07.022.

Watanabe, N., Numakura, T., Sakaguchi, K., Saishu, H., Okamoto, A., Ingebritsen, S., Tsuchiya, N., 2017. Potentially exploitable supercritical geothermal resources in the ductile crust. Nat. Geosci. 10, 140–144. https://doi.org/10.1038/ngeo2879.

Watanabe, N., Yamaya, Y., Kitamura, K., Mogi, T., 2021. Viscosity-dependent empirical formula for electrical conductivity of H2O-NaCl fluids at elevated temperatures and high salinity. Fluid Phase Equilib. 549, 113187 https://doi.org/10.1016/j.fluid.2021.113187.

Watanabe, N., Mogi, T., Yamaya, Y., Kitamura, K., Asanuma, H., Tsuchiya, N., 2022. Electrical conductivity of H2O-NaCl fluids under supercritical geothermal conditions and implications for deep conductors observed by the magnetotelluric method. Geothermics 101, 102361. https://doi.org/10.1016/j.geothermics.2022.102361.

Wespestad, C., Thurber, C., Andersen, N., Singer, B., Cardona, C., Zeng, X., Bennington, N., Keranen, K., Peterson, D., Cordell, D., et al., 2019. Magma reservoir below Laguna del Maule volcanic field, Chile, imaged with surface-wave tomography. J. Geophys. Res. Solid Earth 124, 2858–2872. https://doi.org/10.1029/2018JB016485.

Yoshino, T., Laumonier, M., McIsaac, E., Katsura, T., 2010. Electrical conductivity of basaltic and carbonatite melt-bearing peridotites at high pressures: Implications for melt distribution and melt fraction in the upper mantle. Earth Planet. Sci. Lett. 295, 593–602. https://doi.org/10.1016/j.epsl.2010.04.050.

Zandt, G., Leidig, M., Chmielowski, J., Baumont, D., Yuan, X., 2003. Seismic detection and characterization of the Altiplano-Puna magma body, Central Andes. Pure Appl. Geophys. 160, 789–807. https://doi.org/10.1007/PL00012557.

Zhang, B.H., Guo, X., Yoshino, T., Xia, Q.K., 2021. Electrical conductivity of melts: Implications for conductivity anomalies in the Earth's mantle. Natl. Sci. Rev. 8, nwab064. https://doi.org/10.1093/nsr/nwab064.